Ocean Modelling 168 (2021) 101901

Contents lists available at ScienceDirect

Ocean Modelling

journal homepage: www.elsevier.com/locate/ocemod

Effects of the atmospheric forcing resolution on simulated sea ice and polynyas off Adélie Land, East Antarctica

Pierre-Vincent Huot [a,*], Christoph Kittel [c], Thierry Fichefet [a], Nicolas C. Jourdain [b], Jean Sterlin [a], Xavier Fettweis [c]

[a] Earth and Life Institute, George Lemaitre Centre for Earth and Climate Research, UCLouvain, Louvain-la-Neuve, Belgium
[b] Université Grenoble Alpes, CNRS/IRD/G-INP, IGE, Grenoble, France
[c] Laboratory of Climatology, Department of Geography, University of Liège, Liège, Belgium

ARTICLE INFO

Keywords:
East Antarctica
Katabatic wind
Polynya
Landfast ice
Dense Shelf Water
High resolution

ABSTRACT

Coastal polynyas of the Southern Ocean play a central role in the ventilation of the deep ocean and affect the stability of ice shelves. It appears crucial to incorporate them into climate models, but it is unclear how to adequately simulate them. In particular, there is no consensus on the atmospheric forcing resolution needed to appropriately model the sea ice in coastal Antarctica. A high resolution might be required to represent the local winds such as katabatic winds which are key drivers of coastal polynyas. To fill in this gap, we have tested the sensitivity of sea ice and air-sea-ice interactions to the resolution of the atmospheric forcing in a high-resolution ocean–sea ice model. A set of regional atmospheric simulations at horizontal resolutions of 20, 10, and 5 km are performed with an atmospheric regional model and used to force three ocean–sea ice simulations in the Adélie Land sector, East Antarctica. Due to the better representation of topography with a refined grid, the offshore component of coastal winds becomes stronger at increased resolution. The wind intensification is particularly strong down valleys channelizing the katabatic flow, with increase in wind speed ranging between 1 and 3 m/s. Under a higher resolution forcing, polynyas open more frequently and are wider. This fosters the growth rate of sea ice in polynyas, while landfast ice and pack ice are weakly affected. In polynyas, the production of sea ice is increased by up to 30% at 5 km resolution compared to 20 km resolution. Polynyas downstream of the katabatic wind pathway are more affected than the ones driven by easterly winds, highlighting the importance of the local wind conditions. Brine rejection associated with these higher sea ice production rates affects the salinity budget of the ocean and enhances both the volume and density of the dense Shelf Water produced off Adélie Land. These results underpin the need to better account for local coastal winds and polynyas in ocean and climate models.

1. Introduction

Sea ice growth usually acts as a negative feedback to ocean cooling, as the ice insulates the ocean from the cold atmosphere. However, some processes can inhibit the onset of ice cover, leaving areas of low sea ice concentration called polynyas. These polynyas are often divided into two categories: the sensible heat polynyas, which are forced by anomalously high ocean temperatures inhibiting sea ice freezing, and the latent heat polynyas, which are formed by the local divergence of the sea ice (Morale Maqueda et al., 2004). Most Antarctic coastal polynyas belong to the second category (Massom et al., 1998). They form in recurrent locations, where coastline, grounded icebergs or ice shelf tongues in combination to the wind favor the local divergence of sea ice. Latent heat polynyas host continuous sea ice freezing, which is balanced by wind-driven sea ice export. As polynyas are places of intense air-sea fluxes, they have important effects on the ocean, the ice shelves and fauna of coastal Antarctica. Indeed, brine rejection in polynyas fosters ocean convection and sometimes leads to the formation of Dense Shelf Water (DSW). DSW can latter be transformed into Antarctic Bottom Water (AABW) and thus contribute to the global ocean thermohaline circulation. DSW formed in polynyas can also affect the melting of ice shelves, due to the depletion of the ice melting point at high pressure (Jacobs et al., 1992). Besides, polynyas are often described as "life oases" supporting the planktonic activity (Liniger et al., 2020) and helping Antarctic fauna to endure the harsh winter (Labrousse et al., 2018).

Approximately two thirds of the Antarctic coastal polynyas appear to be driven by katabatic winds (Massom et al., 1998). These winds blow offshore over most of the Antarctic coastline and originate from surface air cooling over the slopes of the Antarctic ice sheet (Parish

* Corresponding author.
E-mail address: pierre-vincent.huot@uclouvain.be (P.-V. Huot).

https://doi.org/10.1016/j.ocemod.2021.101901
Received 26 February 2021; Received in revised form 24 September 2021; Accepted 7 October 2021
Available online 29 October 2021
1463-5003/

and Bromwich, 1987). They are particularly persistent during winter and can reach astonishing velocities such as the yearly mean wind speed of 20 m/s measured by Wendler et al. (1997) at Cape Denison, East Antarctica. Such conditions are favored by the topography which channelizes the katabatic flow. The representation of katabatic winds in atmospheric models relies on their ability to represent the topography and the very stable surface boundary layer over the ice sheet. Polar-oriented regional atmospheric models have been shown to simulate realistic katabatic winds (Jourdain and Gallée, 2011), or to produce stronger coastal winds than a coarse-resolution global atmospheric reanalysis (Mathiot et al., 2012). The ability of atmospheric models to simulate coastal winds is also improved at higher horizontal resolution (Bromwich et al., 2013). Coarse-resolution models (above 1° or 100 km) struggle to represent realistic coastal winds, which can have important implications for the representation of polar climate. The use of high-resolution winds modifies the ocean heat transport towards the Antarctic ice shelves (Dinniman et al., 2015). Introducing katabatic winds in an atmospheric reanalysis modifies the coastal and deep ocean properties (Mathiot et al., 2010; Barthélemy et al., 2012). Besides, Zhang et al. (2015) showed that different treatments of the orographic drag in two atmospheric reanalyses have important repercussions for the simulation of coastal offshore winds and for the coastal sea ice production.

The coarse representation of coastal winds in global climate models might be one of the reasons for their weak convection in coastal areas and biases in AABW properties (Heuzé et al., 2013; Heuzé, 2020). Meanwhile, coarse atmospheric reanalyses are commonly used to force ocean–sea ice models of the Southern Ocean. The new generation of atmospheric reanalyses has a higher horizontal resolution (roughly 30 km in ERA5, Hersbach et al. (2020)), with grid size approaching the 20 km horizontal resolution of the regional atmospheric model used in Mathiot et al. (2012) for instance. While this improves the representation of small-scale atmospheric variability in Antarctica (Tetzner et al., 2019), it remains unclear if this resolution is sufficient to produce realistic coastal ocean and sea ice when used as a forcing for ocean–sea ice models. Petrelli et al. (2008) or Ebner et al. (2014) showed that increasing the atmospheric resolution below 10 km intensifies the katabatic winds and the polynya activity in the Ross Sea sector, but Petrelli et al. (2008) did not involve an ocean–sea ice model. Moreover, the complex topography of the Transantarctic Mountains or the Antarctic Peninsula imposes the use of very high resolution in these regions (2 km in Petrelli et al. (2008)), while it might not be needed elsewhere in Antarctica. The choice of the atmospheric forcing is a primordial question for polar ocean modelers. As high-resolution atmospheric models can be expected to produce more realistic coastal winds and in particular stronger katabatic winds, we expect that increasing the atmospheric forcing resolution could increase the frequency of coastal polynyas and the associated sea ice production.

The Adélie Land sector (East Antarctica) is known for the intensity of its katabatic winds (Wendler et al., 1997). This area is recognized as a major source of AABW (Rintoul, 1998) thanks to the activity of the Mertz Glacier Polynya (see Fig. 1), despite its abrupt decline after the major calving event of the Mertz ice tongue in 2010 (Kusahara et al., 2011b; Tamura et al., 2012; Lacarra et al., 2014; Aoki et al., 2017; Snow et al., 2018). The calving event raised a lot of interest (Cougnon et al., 2017; Kusahara et al., 2017) as the polynya and the ice tongue were suggested to apply strong control on the ocean circulation (Martin et al., 2017). These studies, however, relied on coarse-resolution atmospheric forcing which might underestimate the intensity of katabatic winds. In addition, the representation of sea ice and in particular landfast ice (thick and immobile sea ice fastened to the coastline, to the seafloor, to ice shelf front or to grounded icebergs) remains relatively crude in these models. This is problematic given that landfast ice is thought to be related to the development of coastal polynyas (e.g., Fraser et al. (2012), Nihashi and Ohshima (2015), Fraser et al. (2019)). The blocking of sea ice on obstacles is indeed often a prerequisite for sea ice divergence and the opening of a latent heat polynya. Another interest of the Adélie Land is that it is representative of the majority of Antarctic coastlines, with a relatively smooth topography compared to mountainous areas of Antarctica.

In this study, we aim at investigating whether increasing the resolution of atmospheric forcing beyond the resolution of present global atmospheric reanalyses would affect the activity of coastal polynyas off Adélie Land. To separate the effect of resolution, we use a set of regional atmospheric simulations based on the MAR (Modèle Atmospherique Régional) model at resolutions of 20, 10, and 5 km with consistent physics. These simulations are used to force a regional ocean–sea ice configuration of the NEMO-LIM model (Nucleus for European Ocean Modeling and Louvain-la-Neuve sea Ice Model), including a parameterization of landfast ice. The atmosphere, ocean–sea ice and ice shelf models are described in the second section of this manuscript. In the third section, we analyze how the resolution of the atmospheric model affects the near-surface forcing fields, the sea ice, the polynyas, and the salt fluxes. We finally discuss the implications of fine-scale atmospheric processes for the coastal Southern Ocean and indicate which resolution appears the most suitable for the atmospheric forcing of polar ocean–sea ice models.

2. The model and forcing

2.1. MAR atmospheric model

The MAR model is used to produce the atmospheric forcing of the ocean-sea ice model. MAR is a hydrostatic polar-oriented model (Gallée and Schayes, 1994) that has often been used to study the climate over the Antarctic ice sheet (Amory et al., 2015; Kittel et al., 2018; Agosta et al., 2019; Donat-Magnin et al., 2020; Mottram et al., 2020). The model includes a cloud microphysics module solving conservation equations for five water species: snow particles, cloud ice crystals, rain drops, cloud droplets, and specific humidity (Gallée, 1995). The cloud microphysics module is based on Kessler (1969) parameterizations latter improved following Lin et al. (1983). The MAR radiative scheme has been adapted from the European Centre for Medium-Range Weather Forecasts ERA-40 reanalysis (Morcrette, 2002; Uppala et al., 2005). The transfer of energy and mass between the atmosphere and the surface is simulated by the one-dimensional surface scheme SISVAT (Soil Ice Snow Vegetation Atmosphere Transfer) module (De Ridder and Gallée, 1998). In particular, the module represents the evolution of snow (Gallée and Duynkerke, 1997; Gallée et al., 2001) and ice (Lefebre et al., 2003), partly based on an old version of the snow model CROCUS (Brun et al., 1992). In the surface layer, the turbulence is resolved using the Monin–Obukhov similarity theory, while above the surface layer, it is resolved with a local closure scheme adapted for representing stable conditions in the boundary layer enabling a better representation of katabatic winds (Gallée et al., 2015). The MARv3.10 configuration used in this study is similar to the one without drifting snow evaluated by Le Toumelin et al. (2020) over Adelie Land. MAR describes the atmosphere using a stretched grid with 24 vertical sigma levels, the lowest being at 2 m and 5 are located in the lowest 100 m of the atmosphere. MAR is forced by 6-hourly outputs of ERA5 (Hersbach et al., 2020) at its atmospheric lateral boundaries (pressure, wind, specific humidity, and temperature) and at its sea surface over 2000–2015. The temperature and wind velocity at the top of the atmosphere are constrained by ERA5 following van de Berg and Medley (2016). As MAR is not coupled to an ocean model, it does not simulate sea surface temperature or sea ice concentration, so both are prescribed from ERA5. However, MAR represents the thermodynamical evolution of sea ice energy budget and thickness (with a prescribed minimal value of 10 cm that can be covered by snow). We performed MAR simulations at three resolutions (20, 10, and 5 km) over the same domain covering the NEMO grid (see next section) and using exactly the same parameters for the three runs. In this way, the three simulations share identical physical settings and surface boundary conditions. The results of the three

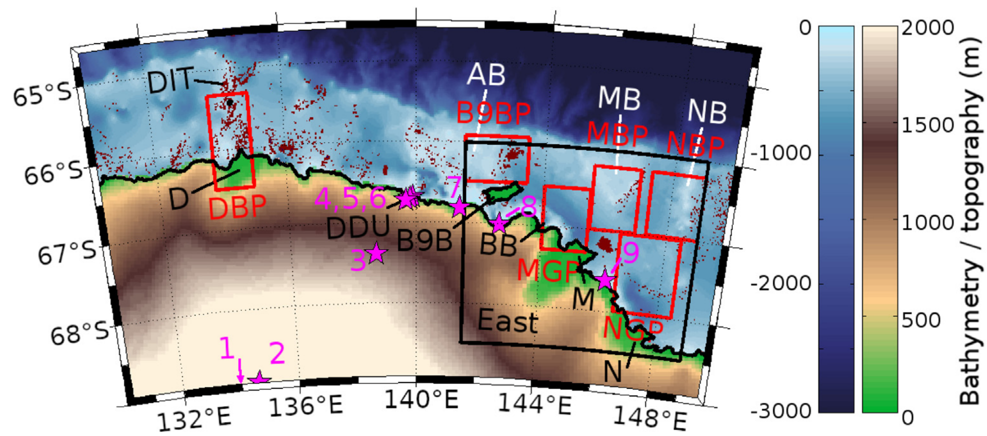

Fig. 1. Bathymetry (in the NEMO-LIM model) and topography (in the AM5 simulation) of Adélie Land and the D'Urville Sea. Dark red dots indicate the locations of small grounded icebergs in the model. Red boxes represent the polynyas of the Dibble Bank (DBP), B9B iceberg (B9BP), Mertz Glacier (MGP), Mertz Bank (MBP), Ninnis Glacier (NGP), and Ninnis Bank (NBP). The black box indicates the area for water mass transformation computation. Pink stars indicate Automatic Weather Stations, 1: D85 (out of the map) 2: E-66, 3: D47, 4: D17, 5: D10, 6: DDU, 7: Port Martin, 9: Cape Denison, 9: Penguin Point. DIT: Dibble iceberg tongue, D: Dibble ice shelf, DDU: Dumont D'Urville base, B9B: tabular iceberg, AB: Adélie Bank, BB: Buchanan Bay, M: Mertz ice shelf, MB: Mertz Bank, N: Ninnis ice shelf, NB: Ninnis Bank.

MAR simulations are described and evaluated in Section 3. Finally, the Antarctic topography and ice and rock fractions are derived from the 1 km resolution digital elevation model Bedmap2 (Fretwell et al., 2013), but unlike previous studies with MAR in Adélie Land (Le Toumelin et al., 2020), the coastline in the three simulations has been corrected to match as much as possible the one from NEMO. This results in adjustments in the ice mask, with notably the removal of the Mertz ice tongue and the addition of grounded icebergs (see below).

2.2. Ocean–sea ice model

We make use of a regional configuration of the NEMO platform (Madec, 2016) in its version 3.6 which includes the sea ice model LIM3.6 (Louvain-la-Neuve sea Ice Model). NEMO-LIM is commonly used to study the whole Southern Ocean (Lecomte et al., 2016; Merino et al., 2016; Marchi et al., 2019) or specific sectors (Jourdain et al., 2017; Donat-Magnin et al., 2017; Hausmann et al., 2020; Huot et al., 2021). The ocean component solves the primitive equations, assuming hydrostatic balance and using the Boussinesq approximation. Parameterizations include a Turbulent Kinetic Energy scheme (Bougeault and Lacarrere, 1989; Gaspar et al., 1990) for vertical mixing. Convection is represented by enhancing vertical mixing. The surface pressure gradient is treated with a time-splitting approach together with a non-linear free surface. The present configuration was used and evaluated against observations in Huot et al. (2021). The grid is refined from the eORCA1 tripolar grid to a resolution of 1/24° in longitude, i.e. from 1.8 to 2.3 km over the domain (130°E-150°E and 60°S-70°S, see Fig. 1). The vertical discretization consists of 75 levels of increasing thickness from 1 m at the top to 200 m at the bottom of the ocean. The thickness of the bottom cells or of the top cells beneath ice shelves is adjusted to match the bathymetry or ice draft. We use a polynomial approximation of the reference Thermodynamic Equation Of Seawater (TEOS-10) [IOC, SCOR, APSO, 2010] optimized for a Boussinesq fluid (Roquet et al., 2015). The sea ice component, LIM3.6, is a dynamic-thermodynamic model described in Vancoppenolle et al. (2009) and Rousset et al. (2015). A subgrid-scale distribution of sea ice thickness with 5 categories is used. Drag coefficients are 5.0×10^{-3} and 1.4×10^{-3} for sea ice–ocean and sea ice–atmosphere, respectively. The simulation of landfast sea ice is achieved following the methodology of Van Achter et al. (2021), also used in Huot et al. (2021). The elastic-viscous-plastic (EVP) rheology was modified to include both isotropic and uniaxial tensile strength based on the works of König Beatty and Holland (2010), Dumont et al. (2009), combined in Lemieux (2016). The isotropic tensile strength parameter k_t is set to 0.2, the eccentricity of the elliptical yield curve e to 1.5 and the number of sub-iterations of the EVP solver to 900. These modifications of the sea ice rheology are not sufficient to adequately represent landfast sea ice off Antarctica. The role of grounded icebergs also needs to be incorporated as suggested by Fraser et al. (2012, 2019), Van Achter et al. (2021). In the model, grounded icebergs are added as anchoring points for the sea ice in the following way: icebergs are treated as land points in the sea ice model and for the surface flux module, but they do not interact dynamically nor thermodynamically with the ocean. The locations of small grounded icebergs (see Fig. 1) were manually extracted from LANDSAT (Landsat image courtesy of the U.S. Geological Survey) images between 2011 and 2015 to build a constant iceberg mask used in the landfast sea ice parameterization.

Surface boundary fluxes are computed every 900 s from the 3 hourly MAR outputs (see next section) using the CORE bulk formulas (Large and Yeager, 2004). An additional freshwater flux representing the melting of icebergs is applied at the ocean surface using the climatology of Merino et al. (2016). No salinity restoring is applied. At the domain boundaries, a flow relaxation scheme (Engedahl, 1995) is applied to the three-dimensional ocean variables and two–dimensional sea ice variables. A Flather scheme (Flather, 1994) is used for barotropic velocities and sea surface elevation. The model simulates under-ice shelf cavities with explicit ocean–ice shelf interactions as implemented in NEMO by Mathiot et al. (2017). The bathymetry of the domain (see Fig. 1) is adapted from the GEBCO dataset (Weatherall et al., 2015), which includes the high-resolution measurements from Beaman et al. (2011). Tides are applied at the lateral boundaries of the domain using the FES2012 dataset (Carrère et al., 2012), as in Maraldi et al. (2013), Jourdain et al. (2019). The bathymetry and ice scape used in the model correspond to the state of the Adélie Land region after the Mertz calving in 2010. More precisely, in our configuration, the Mertz ice tongue is calved and the B9B iceberg is located in the Commonwealth Bay (see Fig. 1). The B9B iceberg is mapped from LANDSAT8 images and represented as a flat ice shelf. B9B iceberg draft is set to 300 m following Mayet et al. (2013). Ice draft and bathymetry under ice shelves are adapted from the Bedmap2 dataset (Fretwell et al., 2013).

2.3. Experimental design

MAR simulations are conducted on three grids with different resolutions (20, 10, and 5 km, respectively simulations AM20, AM10, and AM5). The 3-hourly outputs from MAR are then interpolated on the ocean–sea ice model grid using a bilinear interpolation for scalar atmospheric fields and bicubic interpolation for wind vectors. Before the interpolation, MAR outputs were "drawned", i.e. values over the ice sheet and land points were extrapolated from the nearest ocean points, which limits the effects of mismatch between the ocean model coastline and the coastline in MAR at three different resolutions. These datasets constitute the atmospheric fields used to compute the surface boundary conditions of the ocean–sea ice model via the bulk CORE formulas. Three ocean–sea ice experiments are carried out using the set of atmosphere simulations, namely OM20, OM10, and OM5 (NEMO-LIM forced by AM20, AM10, and AM5, respectively). The simulations start in January 2007 and end in December 2015. The first three years serve as spin-up and are discarded for the sea ice and ocean analysis. Changing the resolution of the atmospheric model impacts the spatial variability of the atmospheric fields, but also modifies the atmospheric model dynamics. In addition, the ocean and sea ice might exhibit different sensitivities to the resolution for each atmospheric variable. To explore in more detail these questions, we ran two additional shorter (2007–2010) simulations. OM20W5 is an ocean–sea ice simulation forced by AM20 apart from the wind speed, which are those of AM5. OM5x20 is forced by AM5 but the high-resolution atmospheric fields were averaged onto the 20 km grid of AM20. The first of these simulations is used to discriminate the sensitivity to the wind resolution from the sensitivity to the resolution of other atmospheric fields, while the second serves to disentangle the dynamical effects from the resolution effects of grid refinement.

3. Atmospheric forcing and effects of resolution

In this section, we describe the differences between the near-surface fields obtained from the three atmospheric simulations AM20, AM10, and AM5. We also compare them to the ERA5 reanalysis to evaluate the atmospheric simulations above the ocean and show the differences between the global reanalysis and the regional polar-oriented atmospheric model. ERA5 has a resolution of 0.28°, which corresponds to approximately 12x31 km near Dumont D'Urville. Simulated surface air temperatures and wind speeds in AM20, AM10, AM5, and ERA5 are compared to those observed by the Automatic Weather Station (AWS) network in Adélie Land in Fig. 2. On every coastal station (Penguin point to Dumont D'Urville (DDU), points 4 to 9 in Fig. 1), MAR exhibits a cold bias, which is slightly reduced in AM5. Inland (E-66 and D-85), MAR simulations show a +1°C bias compared to the AWS. Compared to MAR, ERA5 better represents the mean temperature, which likely results from the assimilation of near-surface temperatures and of radiance and cloud products. The wind speeds simulated by MAR are in better agreement with the AWS observations than winds of ERA5. Both the mean bias and the correlation are improved in MAR. ERA5 exhibits particularly poor correlation and a negative bias reaching 10 m/s for the coastal stations Penguin point and Cape Denison. Increasing the resolution of the atmospheric model tends to improve the simulated wind speeds. Yet, it seems to only partially explain the better performance of MAR compared to ERA5. Indeed, AM20 and ERA5 have similar resolutions, yet AM20 presents more realistic winds. Other source of improvement might be related to the specific treatment of the polar atmospheric boundary layer and surface roughness in MAR (Gallée et al., 2015; Agosta et al., 2019). Coastal winds are better represented in MAR, highlighting the interest of using an atmospheric model developed for the representation of the polar atmosphere to force ocean–sea ice models.

The typical wind conditions of coastal Adélie Land simulated in the MAR runs and ERA5 are shown in Fig. 3. To illustrate the variability of wind conditions blowing over polynyas off Adélie Land, we make the distinction between the easterlies and southerlies cases. To do so, we compute the area-averaged wind direction over the eastern coastal seas (pink box in Fig. 3, corresponding to the area of most intense polynya activity, see Section 4) and use it to discriminate between the easterlies (winds are oriented left of the median wind) and southerlies (winds are oriented right of the median wind). During easterlies periods in AM5 (Fig. 3g), strong winds parallel to the coastline blow over the coastal seas. The mean wind speed intensifies from east to west between 150°E and 140°E, peaking at values of 11 m/s, before weakening west of 132°E. Locally, the mean winds can also show a component perpendicular to the coast in the southeast of the domain, near the Mertz ice tongue, Ninnis ice tongue, or B9B iceberg. The winds perpendicular to the coastlines are of katabatic origin, and the mean wind speeds locally reach 13 m/s there. The average wind conditions during easterlies are similar for the three MAR simulations and for the ERA5 reanalysis (Fig. 3a, c, e, g). Yet, winds tend to be weaker when the resolution is decreased in MAR. For instance, the easterlies blowing north of the B9B iceberg are slower in AM20 than in AM10, the latter being slower than those of AM5. Katabatic winds near the Mertz or Ninnis ice tongues are also weakened at lower resolution. The coastal winds of katabatic origin in the Commonwealth Bay, off the Mertz Glacier and off the Ninnis glacier are stronger in the three MAR simulations than in ERA5. On the contrary, offshore easterlies in ERA5 are stronger than those simulated in the three MAR experiments. Winds in ERA5 are overall stronger than those of MAR, to the exception of the coastal offshore winds in AM10 and AM5. The second mode of wind conditions corresponds to southerlies in the eastern coastal sea (Fig. 3b, d, f, h). During southerlies, the easterlies previously described vanish, and the mean wind speeds over the ocean are lower than in the easterlies case. Despite the overall calm wind conditions, strong winds perpendicular to the coast are encountered near the Ninnis and Mertz ice shelves and in the Commonwealth Bay. There, the wind speeds reach 13 m/s in AM5. The intensity of the local southerlies weakens with decreasing resolution (AM10 and AM20; Fig. 3d, f). Southerlies are weaker in ERA5 than in the three MAR simulations. However, the winds away from the coast are stronger in ERA5 than in the MAR simulations during the southerlies regime. ERA5 near-surface winds are on average stronger everywhere above the ocean away from the coastline. As an increase of resolution tends to strengthen coastal winds but do not affect the winds away from the coast, the difference of resolution between ERA5 and the MAR experiments should not explain the changes of wind speeds over the ocean. The stronger winds in ERA5 might come from differences in the turbulent mixing parameterizations or to the treatment of surface roughness lengths between the atmospheric model of ERA5 and the MAR model. Yet, MAR produces stronger katabatic winds even at low resolution which is probably linked to the specific adaptation of MAR for the modeling of polar climate. The increase in resolution is a second factor explaining the higher katabatic wind speeds in MAR than in ERA5, and also explains the intensification of winds between AM20, AM10 and AM5. In summer (not shown), the wind conditions are similar, with two preferential wind directions (easterlies and southerlies). Summer winds are on average weaker than winter winds. The same differences between the three simulations and reanalysis are found (i.e. in general stronger winds over the ocean in ERA5, but stronger southerly winds along the coast in the MAR simulations).

The intensification and change of direction of coastal winds when comparing ERA5 to the MAR simulations or MAR simulations with different resolutions can be related to the differences in topography. The topographies of ERA5 and of the three MAR simulations are shown in Fig. 4a, c, e, f. The refinement of resolution between ERA5 and MAR, and between AM20, AM10 and AM5 enable a more realistic representation of small-scale structures such as the valleys associated with the Dibble, Mertz or Ninnis Glaciers. A better representation of valleys favors the channelization of the katabatic flow and the subsequent local intensification of those winds (as can be seen in Fig. 3). The peak of katabatic wind intensity observed in Fig. 3 coincides with the location of the Mertz and Ninnis glacier valleys. The increase of resolution to 10 km allows for a much better representation of the valleys compared to AM20 or ERA5, the additional refinement to 5 km leading to minor changes. Besides the representation of valleys, a higher resolution enables to better capture the steep slopes of the

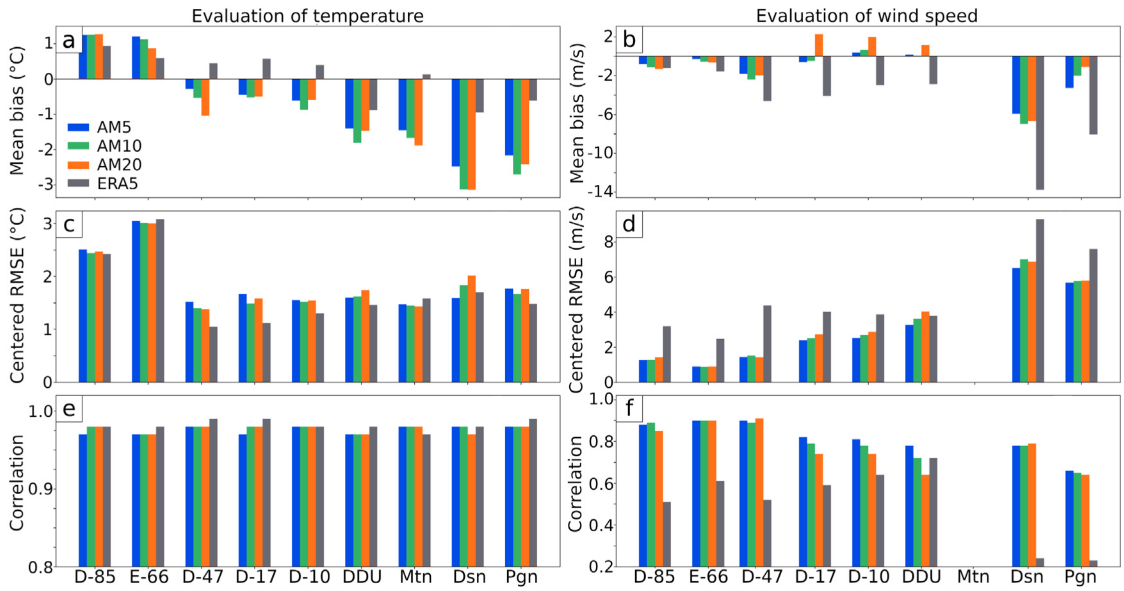

Fig. 2. Mean bias (a) and root mean-square error (RMSE; c) of surface air temperatures simulated in AM20, AM10, AM5, and ERA5 with the measurements performed by the Automatic Weather Station (AWS) network (see Fig. 1 for station locations). (e) Correlations between the surface air temperatures simulated in AM20, AM10, AM5, and ERA5 and the ones measured by the AWS network (all correlations are significant with $p < 0.05$). (b), (d), (f): same as (a), (c), (e) but for wind speed. DDU: Dumont D'Urville, Mtn: Port Martin, Dsn: Cape Denison, Pgn: Penguin Point. Note that no wind data were available for Port Martin.

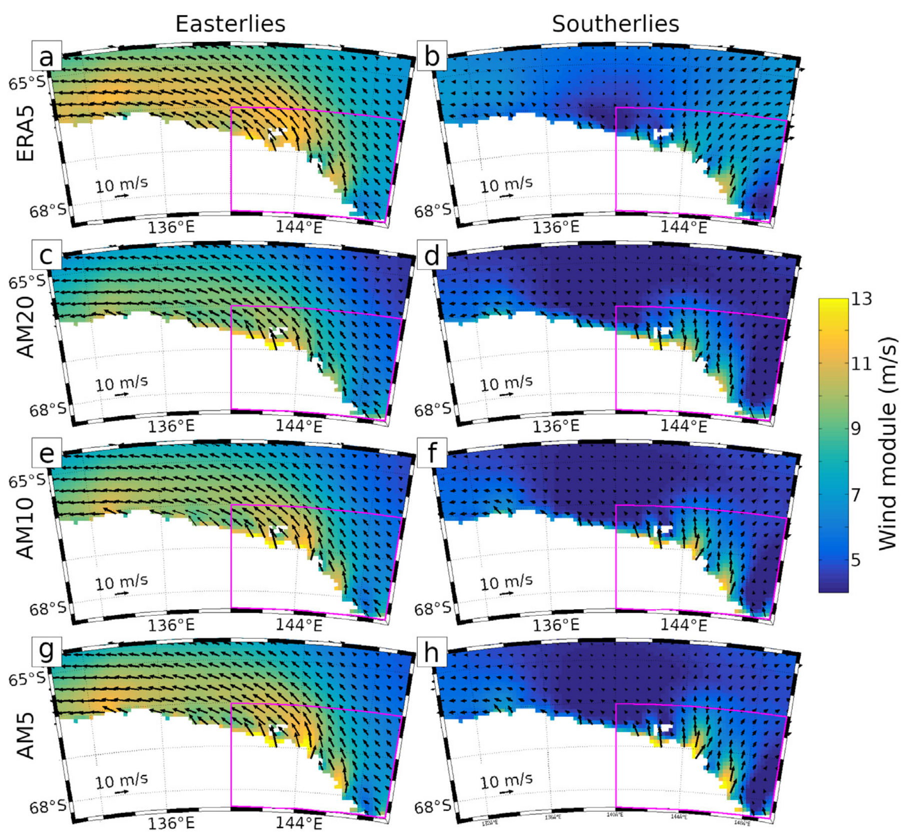

Fig. 3. Mean wind speed during easterlies (left column) events and southerlies (right column) events in winter (May to September), averaged over 2010–2015. (a) and (b): ERA5, (c) and (d): AM20, (e) and (f): AM10, (g) and (h): AM5. Easterlies and southerlies events are defined using the distribution of the area-averaged wind direction over the pink box. Easterlies (southerlies) are defined as events when the area-averaged wind direction is lower (higher) than the median wind direction.

Antarctic Ice Sheet (Fig. 4b, d, f, h). The slopes of the Antarctic Ice Sheet are much smoother in the ERA5 topography than in the one of AM5. The gradual grid refinement between AM20 and AM5 is also accompanied by a steepening of the slopes along the coastline. Steep slopes are important for the acceleration of the gravitational flows such as katabatic winds.

Topography applies a strong control on the coastal winds as can be seen in Fig. 5. In the MAR simulations, the zonal distribution of the

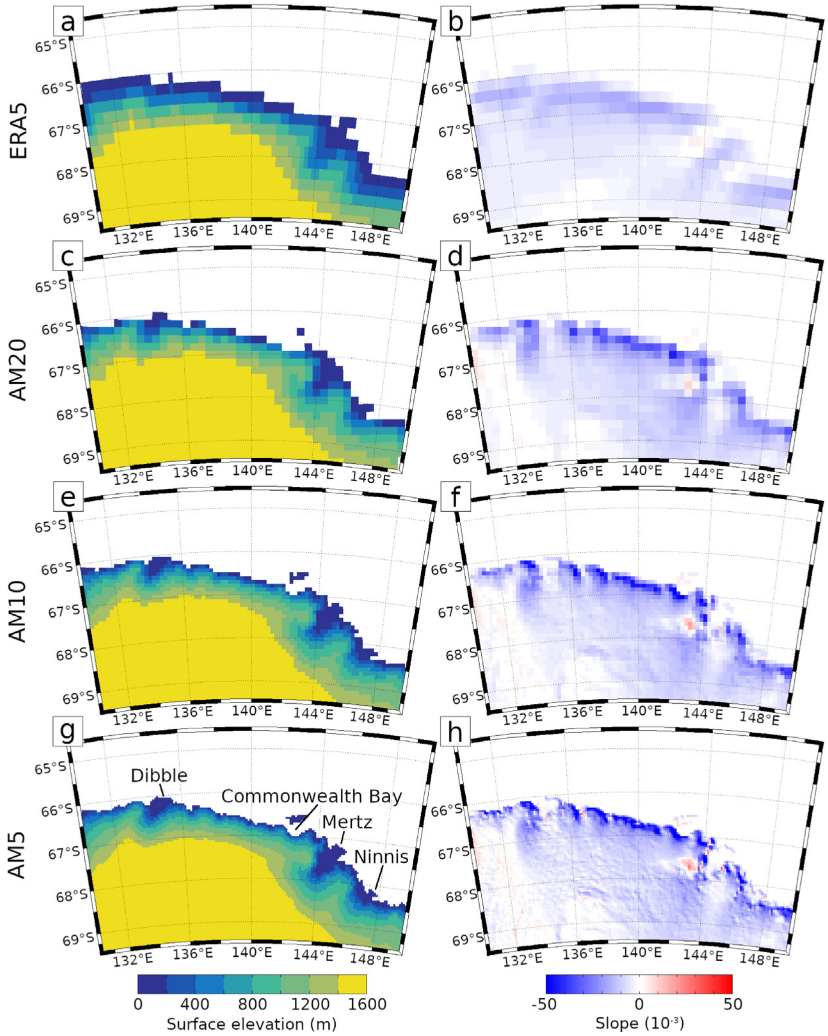

Fig. 4. Topography (left) and terrain slope (right) in ERA5 (a and b), AM20 (c and d), AM10 (e and f), and AM5 (g and h). The terrain slope is counted positive when the surface elevation increases eastward/northward.

intensity of the meridional (offshore) and zonal components coastal winds presents a large variability between 142°E and 150°E. The most notable maximums are found in regions where the topography channelizes the katabatic flow, i.e. in the Commonwealth Bay and off the Mertz or Ninnis valleys (see Fig. 4). The imprint of the Dibble ice shelf also appears on the wind speeds. The intensity of the zonal (easterlies) winds decreases in front of these valleys as the component of katabatic winds that is parallel to the coast is weak. As can be seen in Fig. 3, the intensity of the coastal meridional or zonal winds increase with the resolution: AM5 meridional winds are 1 to 3 m/s faster and zonal winds 1 to 4 m/s faster than those of AM20. The imprint of remarkable topographic features (Mertz and Ninnis valleys, Commonwealth Bay) is much weaker or absent in the ERA5 coastal winds. Two peaks can be seen east of the Commonwealth Bay and Mertz valley, but are of weaker magnitude than those of AM10 or AM5. The control applied to coastal winds by small-scale topographic features is increased with the resolution and is particularly weak in the ERA5 reanalysis.

Increasing the MAR forcing resolution has nearly no effects on the near surface air temperature and humidity, as illustrated by the seasonal cycles shown in Figs. 6a and 6c. The three MAR experiments have similar air humidities over the coastal ocean, and AM5 exhibits a moderate warming (up to 1 °C) compared to AM10 and AM20 in winter. The seasonal cycles of temperature simulated in the three MAR experiments are similar to the one of the ERA5 reanalysis. The atmosphere simulated over the coastal ocean in MAR is moister than ERA5 (from +0.22 g/kg in AM20 to +0.25 g/kg in AM5). The precipitation rate simulated in MAR over the coastal sea increases with the resolution (+0.22 mmWE/day between AM10 and AM20, +0.52 mmWE/day between AM5 and AM20) and are overall higher than those of ERA5 in winter for AM20 and year round for AM10 and AM5. The downward longwave radiation is higher by 2 to 5 W/m^2 between AM5 and AM10 or AM20. Simulated downward longwave radiations are on average higher in winter (+3 W/m^2 in AM20 and AM10, +5 W/m^2 in AM5) and lower in summer in MAR compared to ERA5.

Increasing the resolution of the atmospheric model leads to an intensification of the coastal offshore winds and of easterly winds. Other atmospheric fields are less impacted apart from the precipitation which increases with resolution. The three MAR simulations present several differences with the ERA5 reanalysis that do not originate from changes in resolution (higher air humidity, slower winds above the ocean). As our goal is to understand the role of forcing resolution on the simulation of the ocean and sea ice, we will only use the three MAR experiments as atmospheric forcing. A comparison between an ocean–sea ice simulation forced by ERA5 and the OM20 and OM5 simulations is presented in Appendix A of the supplementary material.

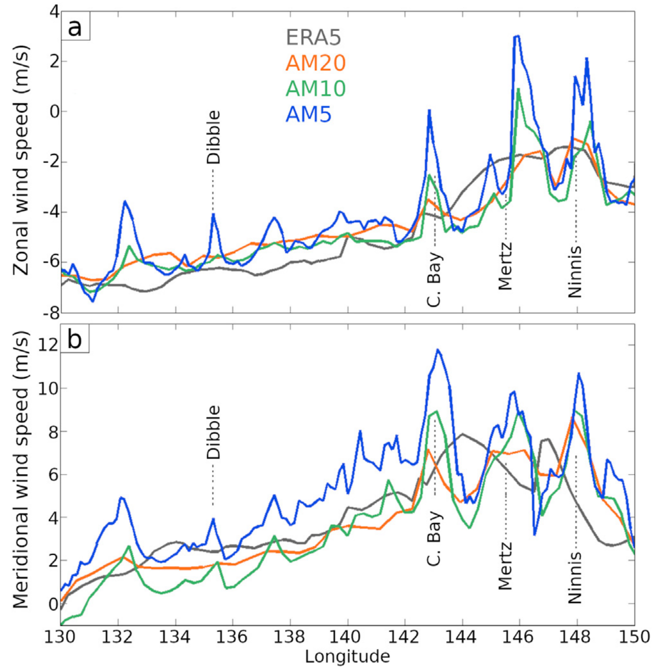

Fig. 5. Zonal (a) and meridional (b) wind speeds at the coast (defined as the first ocean point after the continent) averaged between 2010–2015 (all seasons). Note that the location of the first ocean points varies with the representation of the coastline in the different models. C. Bay: Commonwealth Bay.

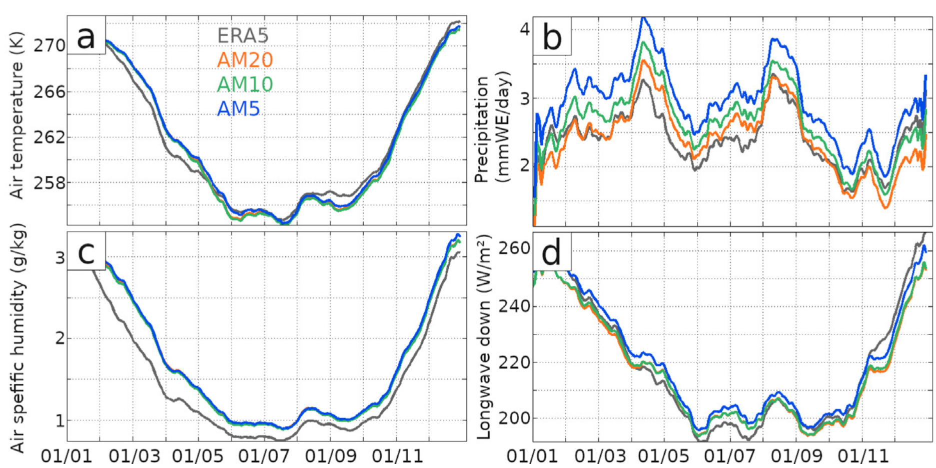

Fig. 6. Seasonal cycle (averaged between 2007 and 2015) of (a) 2 m air temperature, (b) total precipitation, (c) 2 m air specific humidity, and (d) downward longwave radiation simulated in ERA5 global reanalysis and in AM5, AM10, and AM20, averaged over the ocean between 131 to 149°E and 64.5 to 68.5°S.

4. Sensitivity of the ocean and sea ice to the atmospheric forcing resolution

4.1. Effects of the atmospheric forcing resolution on sea ice

In this section, we describe the mean sea ice state in OM5 and show how it is affected by the atmospheric forcing resolution in simulations OM20 and OM10.

First, we evaluate the state of the sea ice cover simulated in OM5 with respect to observations. The observed sea ice concentrations are obtained from the 6.25 km resolution ASI-AMSR-E dataset (ARTIST sea ice dataset developed using data from the Advanced Microwave Scanning Radiometer - Earth Observing System (Spreen et al., 2008)). The time coverage is limited to one year but its high resolution enables the visualization of small-scale features such as polynyas (comparing simulated and observed sea ice concentration on the 2011–2015 period (not shown) yields similar conclusion). The mean sea ice covers simulated in OM5 for summer and winter of 2011 are displayed in Figs. 7a and 7c, respectively. The simulated sea ice concentration shows good agreement with the observations depicted in Figs. 7b and 7d. In summer, the model tends to underestimate the sea ice cover in the eastern part of the domain. The landfast ice patches (areas high sea ice concentration in summer) persist throughout the melt season due to their high thickness. They are well distributed though being larger in the simulation than in the observations. In winter, several polynyas appear over the continental shelf. The model is able to represent their location but underestimates their extent, especially for the DBP and for the polynya off the Dumont D'Urville base (140°E). The misrepresentation of polynyas might be due to the iceberg mask built in this study, as the iceberg distribution is assumed to be constant during the simulated period. The simulated winter sea ice thickness is compared to the sea ice thickness retrieved using a combination of Cryosat-2 and AMSR2 altimeters in the LEGOS/CTOH dataset (Guerreiro et al., 2017) (LEGOS: Laboratoire d'Etude en Géophysique et Océanographie Spatiale, CTOH: Center for Topographic studies of the Ocean and Hydrosphere). The range of sea ice thickness and its spatial variability are well captured

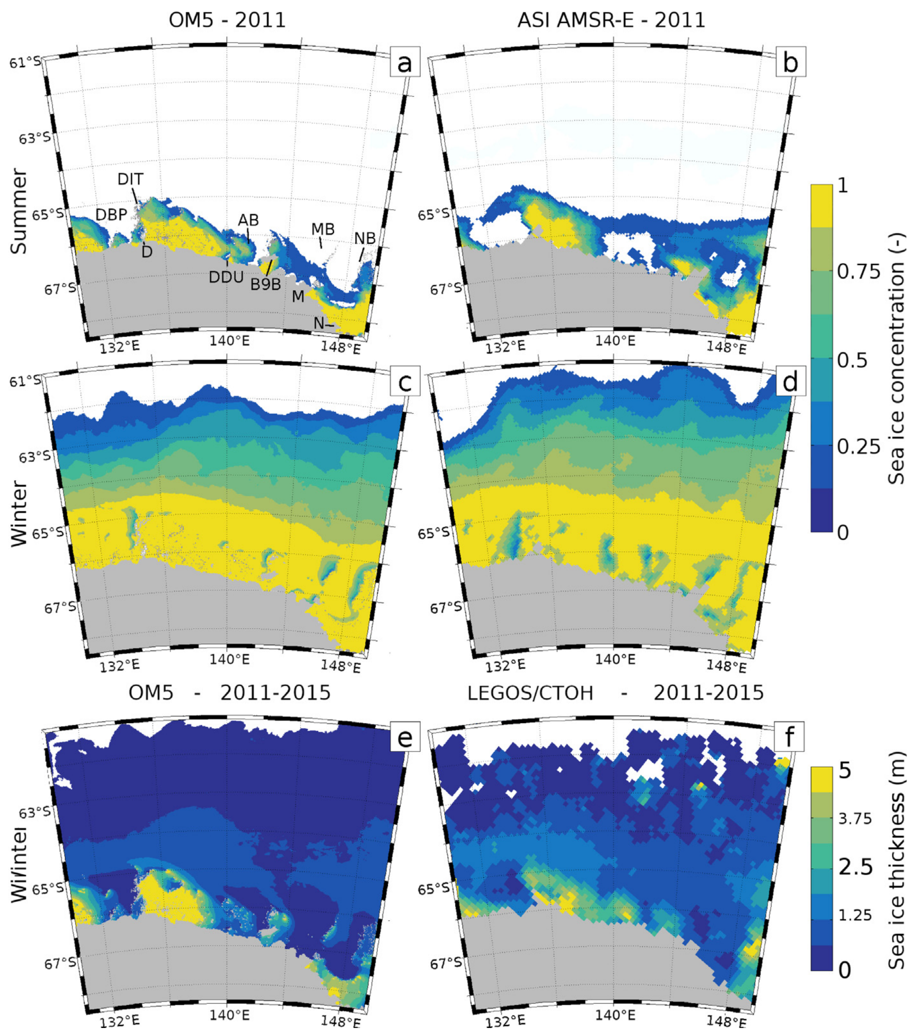

Fig. 7. Sea ice concentrations simulated in OM5 and observed in ASI AMSR-E during summer (a and b) and winter (c and d) of 2011. Sea ice thickness averaged during winters of 2011–2015 as simulated in OM5 (e) and observed in the LEGOS/CTOH Cryosat-2 AMSR2 dataset (Guerreiro et al., 2017) (f). Year 2010 is discarded as we use the post-calving (after 2010) ice scape in our model. DIT: Dibble iceberg tongue, D: Dibble ice shelf, DDU: Dumont D'Urville base, AB: Adélie Bank, B9B: tabular iceberg, M: Mertz ice shelf, MB: Mertz Bank, N: Ninnis ice shelf, NB: Ninnis Bank.

by the OM5 simulation (Figs. 7e and 7f). For instance, the landfast ice patches can be identified by sea ice thicker than 2 m. The thickness of the landfast ice patch at 136°E is overestimated in the model with values reaching 6 m and even 8 m locally. Such thick sea ice can also be observed in the LEGOS/CTOH dataset but it covers smaller areas.

The heterogeneity of the coastal sea ice off Adélie Land is a major driver of the spatial variability of air-sea heat fluxes. The simulated sea ice cover can be decomposed in two distinct types of sea ice: landfast ice and polynyas (Figs. 8a and 8b). The thick sea ice cover inhibits air-sea fluxes in landfast ice patches, which is not the case in polynyas. In the OM5 simulation, landfast ice patches are found year-round east of the Dibble iceberg tongue (east of 135°E), south of the B9B iceberg (142°E), or east of the Mertz glacier tongue. The landfast ice cover is intermittent in other regions such as the Adélie or Ninnis Banks. Polynyas frequently open in the lee of obstacles and landfast ice patches. Six important polynyas can be identified: west of the Dibble iceberg tongue (DBP), north of B9B iceberg (B9BP), north of the Mertz Glacier (MGP) or Ninnis Glacier (NGP), and above the Mertz Bank (MBP) and Ninnis Bank (NBP) (see Fig. 1 for polynya names used throughout the manuscript). These polynyas can also be seen in the observations of sea ice concentration of Fig. 7d. Increasing the resolution of the atmospheric forcing from 10 to 5 km (Figs. 8c and 8d) leads to a localized decrease in landfast ice probability and to an enhanced probability of polynya opening. Areas where landfast ice cover is intermittent undergo a decrease in landfast ice cover probability, while persistent patches are unaffected. Polynyas become more frequent under higher resolution forcing, with strongest changes in coastal polynyas. The differences between OM20 and OM5 show the same spatial distribution as the differences between OM10 and OM5, but the magnitude of the changes is increased. Areas frequently occupied by landfast ice are replaced by polynyas, such as the lee of the B9B iceberg or the Buchanan Bay (west of the Mertz ice tongue). Increasing the forcing resolution locally reshapes the contours of the sea ice cover in coastal seas, reducing the landfast ice cover and favoring the development of polynyas due to the strengthening of winds. Increasing the resolution thus improves the representation of polynyas, as the OM5 simulation tends to underestimate their extent (Fig. 7).

The simulated sea ice production (Fig. 9a) closely matches the locations of polynyas. In addition, the shelf break appears to be a favorable place for sea ice production. Compared to the AM10 forcing, the AM5 one leads to enhanced sea ice growth rates inside the polynyas (Fig. 9b). This can be attributed to the increase in polynya extent and frequency, but also to the intensification of turbulent surface heat fluxes due to the increase in wind speed. The sea ice growth rates of OM5 are much higher than those of OM20 inside the polynyas (Fig. 9c). Moreover, in OM5, sea ice growth rates also appear higher in landfast ice patches. On the contrary, the sea ice production north of the shelf

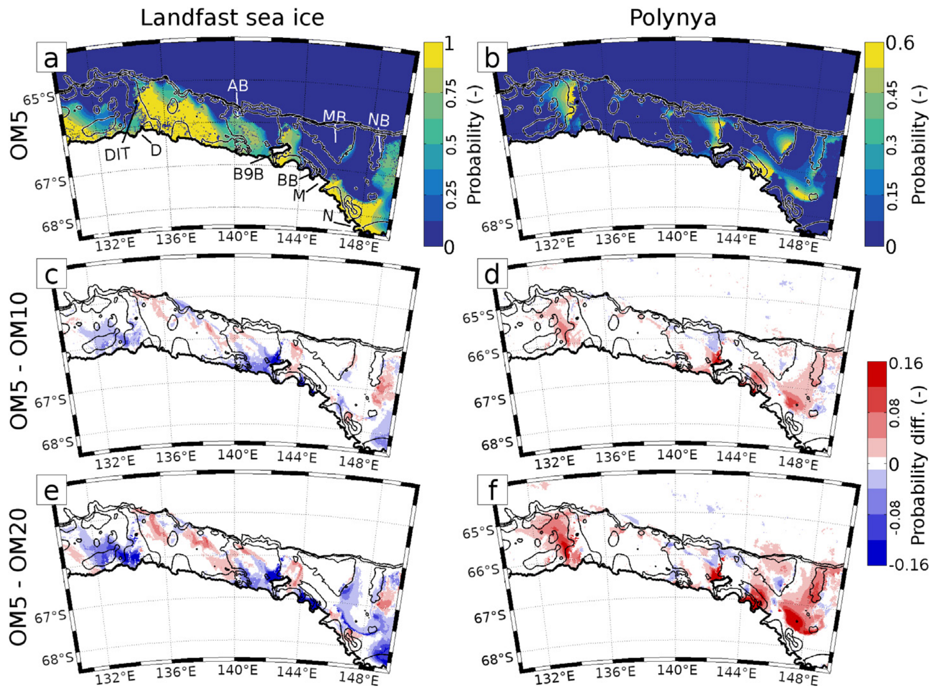

Fig. 8. Probability of landfast ice (a) and polynya (b) occurrence in OM5 averaged between years 2010 to 2015. Difference of landfast ice (c) and polynya (d) probability between OM5 and OM10. Difference of landfast ice (e) and polynya (f) probability between OM5 and OM20. Landfast ice is defined as sea ice with a 15 day averaged velocity lower than 0.1 cm/s. Polynyas are defined as closed contours within the ice pack with a daily sea ice concentration lower than 15% or a daily thickness lower than 0.2 m. Bathymetry is represented as black contours every 400 m. Legends for the panel (a) DIT: Dibble iceberg tongue, D: Dibble ice shelf, AB: Adélie Bank, B9B: tabular iceberg, BB: Buchanan Bay, M: Mertz ice shelf, MB: Mertz Bank, N: Ninnis Glacier, NB: Ninnis bank. Legends for panel (b): DBP: Dibble Bank polynya, B9BP: B9B iceberg polynya, MGP: Mertz glacier polynya, MBP: Mertz Bank polynya, NGP: Ninnis glacier polynya, NBP: Ninnis Bank polynya.

break is lower in OM5 than in OM20. The lower offshore sea ice production in OM5 can be a consequence of the higher ice production rates on the shelf seas which inhibits air-sea exchanges downwind.

The effects of the atmospheric forcing resolution on individual sea ice growth processes are illustrated in Figs. 9d to 9o. The open-water freezing term (Figs. 9d to 9f) refers to the formation of new sea ice in ice-free ocean. Open-water freezing is responsible for intense sea ice formation concentrated on the upwind sides of the polynyas and vanishes after a few kilometers. This process is strongly affected by the forcing resolution: switching from AM10 to AM5 or from AM20 to AM5 both yield an intensification of the open-water sea ice production (though being larger in the second case). Open-water ice formation is lower at high resolution in a few places (Fig. 9f), which can be explained by the displacement of the landfast ice edges under higher-resolution forcing (see the previous section). After its formation, sea ice can grow through several mechanisms. The dominant term is the bottom growth through the freezing of seawater (Figs. 9g to 9i). This process is more intense for the newly-formed, thin sea ice, than for thicker sea ice as the latter inhibits the ocean heat loss. Bottom growth is responsible for important rates of sea ice production in polynyas, downwind the areas of open water formation, and also significantly contributes to sea ice growth at the shelf break. Bottom freezing inside polynyas is enhanced under-higher resolution forcing. On the contrary, it is reduced in AM5 compared to AM20 in landfast ice patches. Another mechanism of sea ice growth is snow-ice formation (Figs. 9j to 9l). When the snow load on top of sea ice becomes too heavy, the snow-ice interface is depleted beneath the sea surface. Seawater then floods the porous snow and freezes in-situ. Sea ice growth by snow-ice formation is dominant for landfast ice patches and sea ice north of the shelf seas, but almost null in polynyas (since newly formed sea ice has not accumulated snow yet). Snow-ice formation is enhanced when the forcing resolution increases, both between OM5 and OM10 and between OM5 and OM20. Higher snow-ice formation rates are found in landfast ice and in offshore pack ice. This enhancement certainly results from the lower precipitation in the low-resolution version of MAR (Fig. 6). Finally, the ridging and rafting induced by sea ice convergence can also lead to sea ice formation. During its deformation, the porosity of the sea ice increases enabling the entrapment of seawater. The entraped seawater can later freeze in-situ. This process is referred to as "dynamical growth" and is illustrated in Figs. 9m 9o. The dynamical growth is maximum upwind of landfast ice patches or grounded icebergs. Its contribution to the sea ice growth is small, but it is increased when using high-resolution forcing. This might be one of the reasons for the slight increase in landfast ice probability found at the edges of the landfast ice patches under higher-resolution forcing (Figs. 8c and 8e).

The contributions of individual sea ice growth term (i.e., open-water freezing, bottom freezing, snow-ice formation, and dynamical growth) and melting terms to the yearly sea ice budget are shown in Fig. 10. As the sea ice cover is highly heterogeneous, the distinction is made between landfast ice, polynya sea ice, and “pack” ice. Landfast ice and polynya ice are defined as in Fig. 8 (i.e. using a velocity criteria for landfast ice and a concentration and thickness criteria for polynya ice). The “pack” ice represents all the sea ice which is neither landfast ice nor polynya ice. Sea ice growth in polynyas is dominated by new sea ice formation in open water, with a non-negligible contribution of bottom sea ice growth. The latter is the dominant term in pack ice production, followed by snow-ice formation and open-water freezing. Snow-ice formation and bottom growth are the main contributors to landfast sea ice vertical growth. Sea ice melt is governed by basal melting in the three types of sea ice cover, with a secondary contribution of surface melt. Lateral melt is only effective in the pack ice. Increasing the forcing resolution enhances the dynamical, snow ice, and open water production terms, and also strengthens the basal melt (as overall, more sea ice is available for melting in summer). In polynyas, the increase in forcing resolution boosts the open water freezing term, whilst leaving the other terms unchanged. Landfast ice growth slightly increases under high-resolution forcing due to an increase in snow-ice formation and dynamical growth. Changes in snow-ice formation on landfast ice or “pack” ice can be imputed to the higher precipitation rates as the resolution of the atmospheric forcing increases.

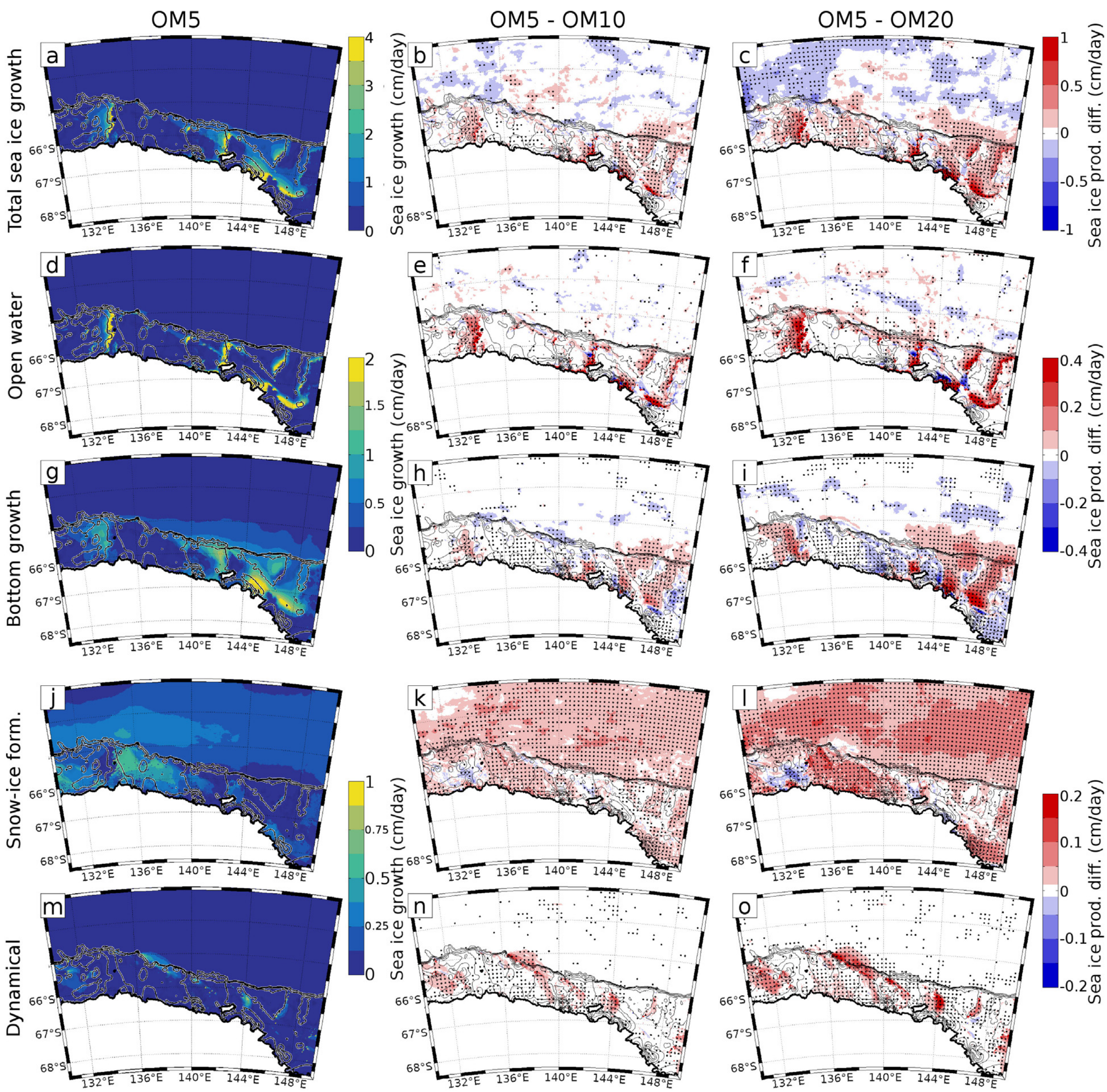

Fig. 9. Mean daily total sea ice production in OM5 (a), difference with OM10 (b), and with OM20 (c). (d), (e) and (f): same as (a), (b), (c) but for open water sea ice production; (g), (h) and (i): bottom sea ice growth; (j), (k), (l): snow-ice formation. (m), (n), (o): dynamical (ridging and rafting) growth. Note the changes in the color axis range as sea ice growth mechanisms have distinct magnitudes. The maps were produced by averaging the sea ice production terms over fall and winter (April–September) 2010–2015. Black crosses indicate statistical significance (2σ). Thin black contours indicate bathymetry (every 200 m).

4.2. Polynya dynamics and sensitivity to atmospheric forcing resolution

Increasing the atmospheric forcing resolution mostly affects the sea ice production inside polynyas, as shown in Figs. 9 and 10. Moreover, the coastal polynyas seem more sensitive to an increase in forcing resolution than the polynyas located farther offshore. To understand this difference, we compare a coastal polynya and an offshore polynya, namely the MGP and the MBP. The seasonal and interannual variability of sea ice production in these two polynyas is displayed in Fig. 11. Sea ice production is increased in OM5 compared to OM10 and OM20, and this throughout all the freezing period and for every year. The MGP (Fig. 11b) shows higher sensitivity to forcing resolution than the MBP (Fig. 11a). The annual sea ice production is 25.8% (8.7%) higher for the MGP and 12.4% (6.6%) higher for the MBP in OM5 compared to OM20 (respectively OM5 and OM10). The higher sensitivity of the MGP to forcing resolution can be explained by its proximity to the coast, where the katabatic winds are particularly intensified at high resolution. The estimates of Tamura et al. (2016) are also shown for the period 2010–2013. The estimated yearly sea ice productions are higher than the simulated ones for the MBP and lower for the MGP. Sea ice production estimated by Tamura et al. (2016) shows two peaks in early fall and late spring for the MBP which are absent from the simulations. The peaks of sea ice production in the early or late freezing season can be related to the hypothesis made by Tamura et al. (2016) who assume that seawater is at freezing temperature, which is probably not the case in late spring and early fall, i.e. when shortwave radiation is non-zero. In the core of winter, estimated and simulated production rates are in better agreement for the MBP, while the MGP produces more sea ice in the simulations.

The distinct sensitivities of the coastal (MGP) and shelf (MBP) polynyas are mainly due to the strengthening and change in direction of the winds in AM10 and AM5 compared to AM20. Figs. 12c and 12d illustrate the probability density distribution of the wind direction θ averaged over the MBP and MGP boxes (θ is the angle between

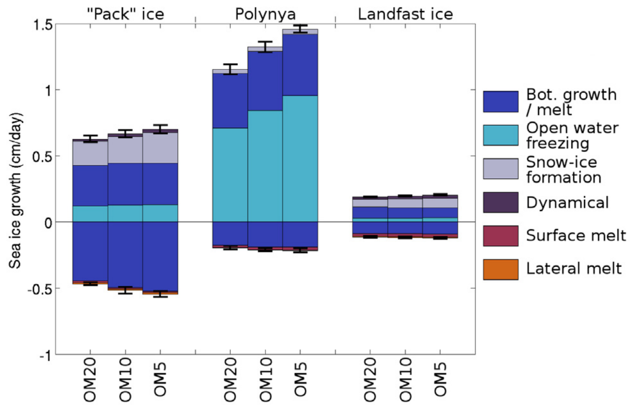

Fig. 10. Yearly mean sea ice production and melting terms simulated in OM20, OM10, and OM5 for three types of sea ice cover. Landfast ice and polynyas are defined in the same way as in Fig. 8. "Pack ice" consists of ice-covered regions that are neither polynyas nor landfast ice. The period is 2010–2015. The interannual standard deviation of the yearly sea ice growth and melt rates are indicated on the top and bottom of each bar.

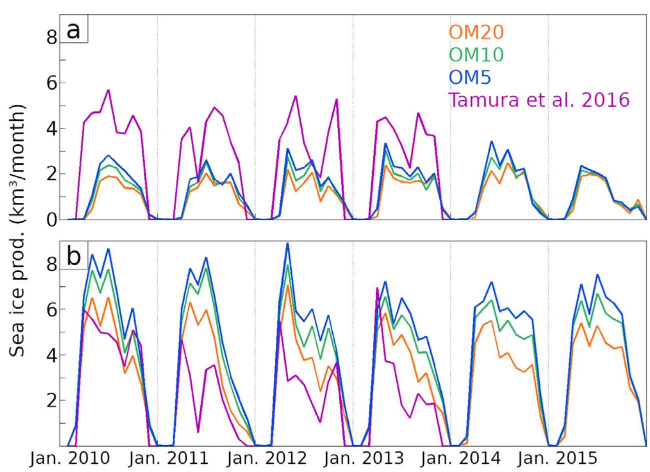

Fig. 11. Sea ice production summed over (a) the MBP (see Fig. 1) and (b) the MGP as simulated in OM20, OM10, and OM5, and as estimated by Tamura et al. (2016) (computed using ERA-interim). Simulated sea ice production is the sum of open-water freezing and bottom growth of sea ice thinner than 0.2 m to approach the methodology of Tamura et al. (2016).

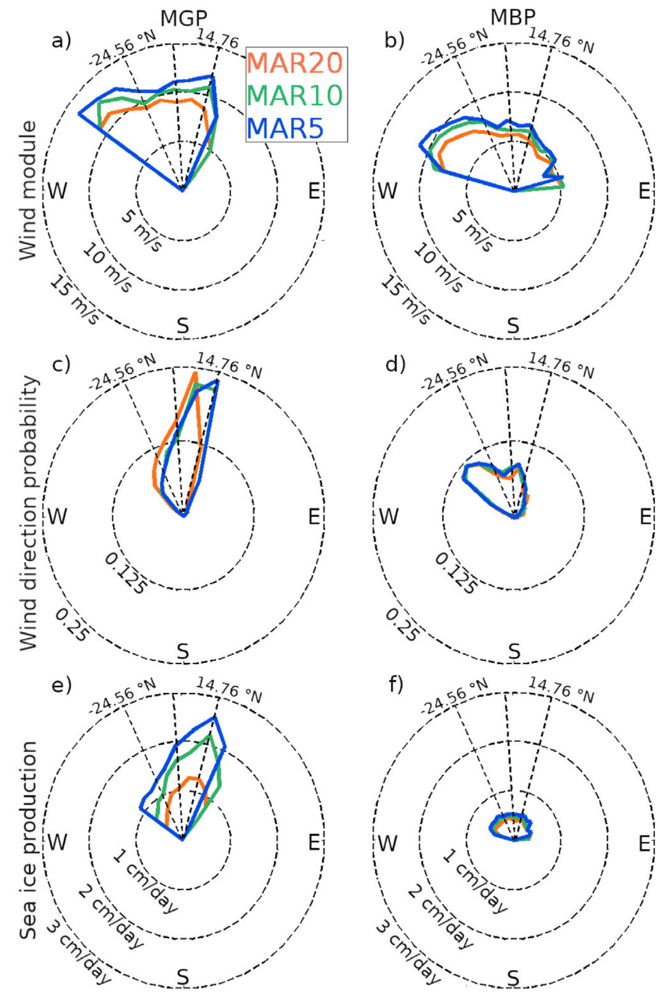

Fig. 12. Averages of the 3-hourly 10 m wind speeds as a function of wind direction simulated in AM20, AM10, and AM5 during winters of 2010–2015 (a), normalized probability density function of the 3-hourly 10 m wind direction θ (c), and sea ice production as a function of wind direction (e) averaged over the MGP. (b), (d), (f): as for (a), (c), (e) but for the MBP. A wind direction of 0°N denotes a southerly wind. The distribution are computed using a bin width of 5°. Bins representing less than 0.5% of the events were removed from the panels (a), (b), (e) and (f) for clarity.

the wind vector and the north, counted positive towards the east). In all experiments, southeasterlies are the most frequent winds over the MBP, with a preferential direction of $\theta = -45°$ and a secondary peak towards 10°. Over the MBP, the wind direction distribution is quite homogeneous between −45° and 15°, suggesting an equal influence of the easterlies and katabatic winds. Winds show a shift towards the east in AM5 compared to AM20. Associated with the change in direction, the intensity of the wind increases with the forcing resolution for both polynyas (Figs. 12a and 12b). Winds are intensified with resolution regardless of the wind direction. The sea ice production in polynyas (hereafter polynya productivity) is depicted in Figs. 12e and 12f. The productivity of the MBP peaks during easterly wind events, while it is maximum for southerly winds in the MGP ($\theta = 15°$). The intensification of winds at high resolution leads to enhanced sea ice production in polynyas. However, this effect is stronger for the MGP than for the MBP as winds favorable to the MGP productivity are more frequent in the high-resolution forcing.

The different wind regimes over the eastern D'Urville Sea are illustrated in Fig. 13. Each wind regime is defined as the mean wind pattern averaged for one quartile of the wind direction distribution over the MGP in AM5 (Fig. 12b). The transition from the easterlies case (1st quartile) to the westerlies case (4th quartile) is accompanied by an overall decrease in area-averaged wind speed, a decrease of northern polynyas productivity (B9BP, MBP, and NBP), and an increase in southern polynyas productivity (MGP and NGP). Easterly winds are indeed less favorable to the opening of coastal polynyas, as they push sea ice towards the coast. Southerlies or westerlies, however, support the northward expansion of the MGP and NGP. In the 3rd and 4th quartiles, katabatic winds dominate the weaker large-scale winds, favoring the opening of the southern polynyas. This suggests that the MGP and NGP are primarily driven by katabatic winds, while the B9BP, MBP, and NBP are rather driven by the easterlies. In addition to the increase in wind speed at high resolution, the shift in direction might also explain the local increase in sea ice production, particularly strong for the MGP and NGP.

Fig. 14 sums up the sensitivity of the wind and sea ice production for the main polynyas off the Adélie Land coast (see Fig. 1). While the winds over the DBP and B9BP are only slightly sensitive to the atmospheric model resolution, all four eastern polynyas (MGP, MBP, NGP, and NBP) undergo an approximate 15% wind increase between the AM20 and AM5 forcings. The MGP, NGP, NBP, and DBP have a strong sensitivity to the atmospheric forcing resolution, with a sea ice production and polynya extent increase by up to 30% between OM20

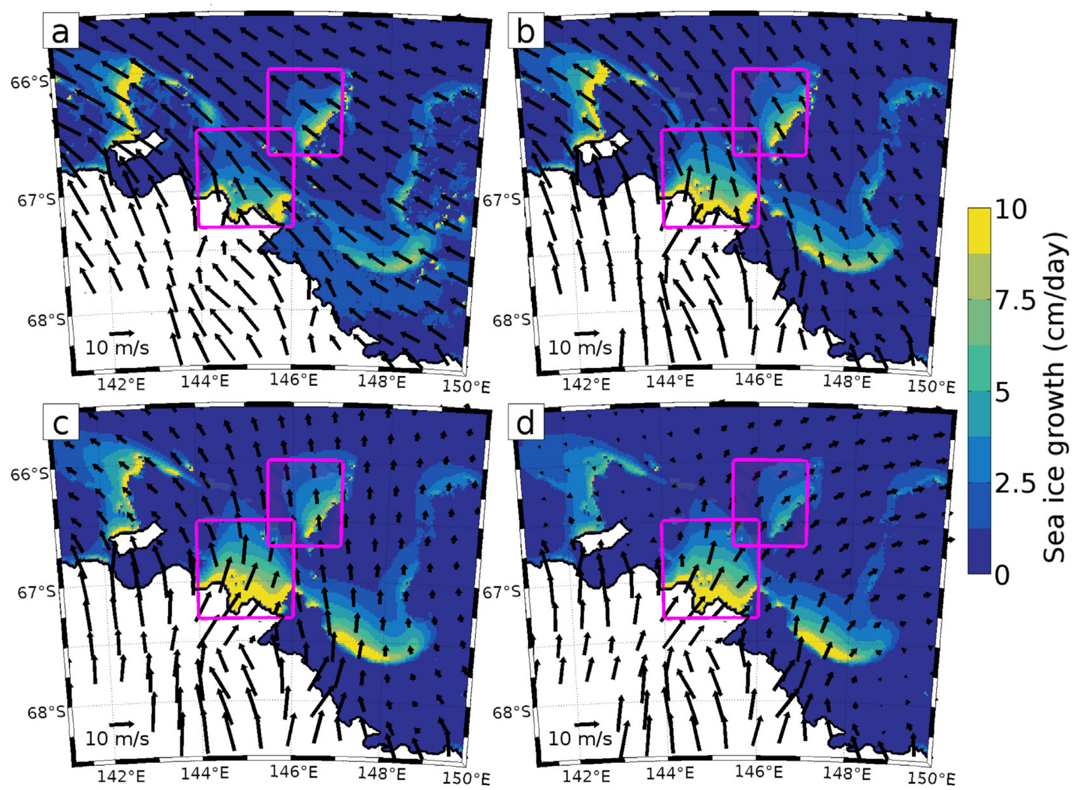

Fig. 13. 10 m daily wind vectors and sea ice growth rates averaged over each quartile of the wind direction distribution of the MGP in AM5/OM5. The maps and quartiles are built using fall–winter (May to September) data from years 2010 to 2015. (a) 1^{st} quartile ($\theta < -24.56°$N), (b) 2^{nd} quartile ($-24.56°\ N < \theta < -3.89°$ N), (c) 3^{rd} quartile ($-3.89°$N $< \theta < 14.76°$ N) and (d) 4^{th} quartile ($\theta > 14.76°$N). Pink boxes indicate the MBP (north) and MGP (south).

and OM5. On the contrary, the B9BP and the MBP experience a weaker sensitivity to the forcing resolution with an intensification of sea ice production by 10%. The lower sensitivity of the B9BP to the increase of resolution can be explained by the weaker increase in wind speed over the B9BP than for the other polynyas. For the MBP, the wind increase has the same magnitude as for the MGP, but the intensification of wind with resolution is accompanied by an increase in southerly wind frequency, which is detrimental to sea ice production in the MBP (see Figs. 12 and 13). Higher sea ice advection from southern polynyas can also inhibit the sea ice growth in polynyas located downwind, limiting the sensitivity of northern polynyas to a wind intensification. Coastal polynyas (MGP and NGP) forced by katabatic winds are more sensitive to the change in wind intensity and direction associated with the refinement of the atmospheric model grid than polynyas located further offshore. The comparison of the sea ice production in polynyas and of the polynya extent between the three simulations reveals that the use of AM10 instead of AM5 has a weaker impact than the use of AM20 instead of AM5. The sea ice production is decreased by 3 to 10% (except from the 15% of the NGP) between OM10 and OM5, and by 5 to 33% between OM20 and OM5 suggesting a limitation of the effect of the forcing resolution below 10 km.

Increasing the atmospheric model resolution affects the spatial variability of the forcing fields and the atmosphere dynamics. To disentangle these two effects, the experiment OM5x20 is used (ocean–sea ice simulation forced by AM5 averaged on the AM20 grid). In addition, the sensitivity of the polynyas to the forcing resolution may differ from one atmospheric field to the other. The sensitivity of the polynyas to an increase in the resolution of the wind is tested in OM20w5 (simulation forced by the winds of AM5 and other atmospheric fields from AM20). The polynya area and productivity simulated in these two experiments are compared to those of simulations OM20 and OM5 in Fig. 15. For most polynyas, the sea ice production and polynya area in OM5x20 and OM20w5 are similar to those of OM5. The fact that OM5x20 does not strongly differ from OM5 suggests that most of the effect of the resolution arises from the modification of the atmospheric model dynamics, i.e., from the intensification and change of direction of the coastal winds. It can be noted that the size and the sea ice production of the NGP vary quite substantially between these experiments. The NGP appears to be sensitive to the small-scale winds (smoothed in OM5x20) or to the increase of resolution for other atmospheric fields than the winds. The NGP is subjected to intrusions of warm modified Circumpolar Deep Water from the east. Slight changes in the local wind divergence or curl due to the coarsening of the AM5 winds onto the AM20 grid might affect the transport of mCDW into the NGP but not in the other polynyas. Increasing only the resolution of the wind and not that of the other atmospheric fields (simulation OM20w5) yields similar results than OM5. These results show that very high resolution matters less than simulating adequate wind speed and direction, although a high-resolution atmospheric model may be required to produce adequate winds.

5. Effects of atmospheric forcing resolution on salt flux and water mass transformations

The increase in atmospheric forcing resolution enhances the sea ice production in the coastal seas off Adélie Land, thanks to the increase in polynya frequency. Due to the brine released during sea ice freezing, such changes might have important repercussions for the salt budget and water mass transformations off Adélie Land. Fig. 16a shows the salt budget associated with sea ice freezing or melting cumulated over the entire Adélie Land sector. The simulations exhibit a positive salt budget in the first 200 km from the coastline. Several peaks corresponding to the polynyas and the shelf break can be identified. Further offshore, the salt budget is negative. The Adélie Land sector is a region of net production and export of sea ice, as the positive salt flux is not entirely compensated by the negative one. Increasing the atmospheric forcing

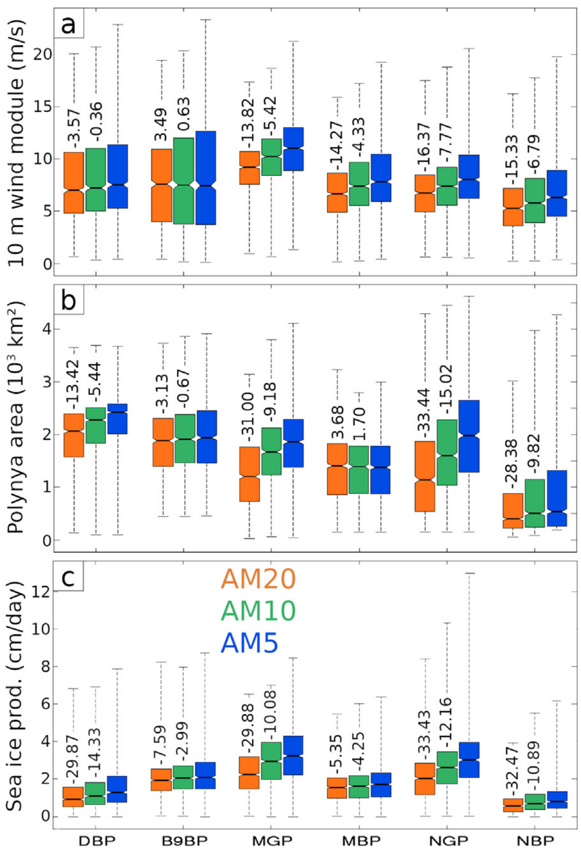

Fig. 14. Distribution of (a) daily 10 m wind speed, (b) polynya area and (c) sea ice growth rate averaged over polynyas off Adélie Land (see Fig. 8b for polynya definition), as simulated by OM20, OM10, and OM5 (respectively AM20, AM10 and AM5 for atmospheric fields) during winters of 2010–2015. Horizontal black lines indicate the median values; the top and bottom of the bars correspond to the 75th and 25th percentiles, respectively. The maximum to minimum range is depicted by the dashed whiskers. The averages of the relative difference between coarse-resolution experiments and OM5 (resp. AM5 for winds) are listed as percentages above the boxes.

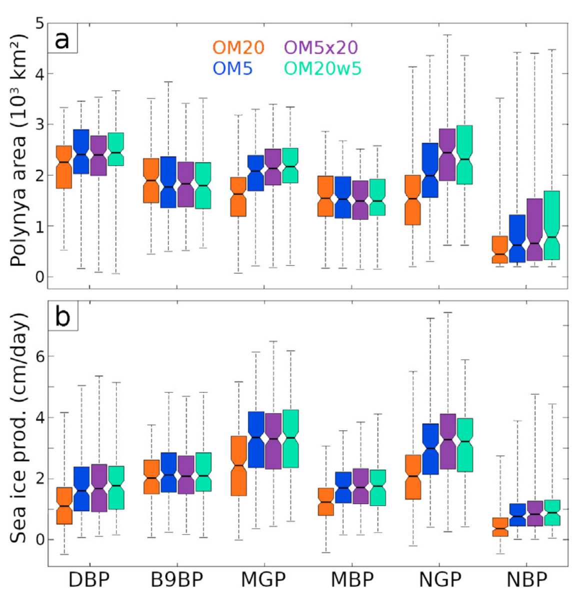

Fig. 15. Same as Figs. 14b and 14c for years 2009–2010, including sensitivity experiments OM20w5 and OM5x20.

resolution substantially affects the amount of salt being rejected into the ocean in the first 200 km from the shore. Switching from AM20 to AM5 and from AM10 to AM5 increases the near-shore salt flux by 17% and 5.9%, respectively.

Another key process associated with polynyas is the production of Dense Shelf Water, potentially feeding the deepest limbs of the global ocean circulation. The water mass transformation rates are computed in the box "east" of Fig. 1 for the experiments OM20, OM10, and OM5. To calculate these rates of transformation, we follow the methodology of Abernathey et al. (2016), also used in Jeong et al. (2020). A potential density scale is defined, ranging from 24.9 kg/m^3 to 28 kg/m^3, with decreasing density step from 0.1 kg/m^3 to 0.01 kg/m^3 in order to refine the resolution on the high-density end. The buoyancy flux associated with brine rejection is used to derive a water mass production rate for each density class previously defined. The transformation of Dense Shelf Waters (waters with a potential density of 27.80 kg/m^3) is 0.39 Sv in OM5 (Fig. 16b). Williams et al. (2008) estimated that 0.1 to 0.5 Sv of Dense Water outflowed the Adélie Depression at the Adélie Sill. Note that our estimate integrates a broader area than the Adélie Depression and that Williams et al.'s estimates were performed prior to the breaking of the Mertz ice tongue.

The production of water masses with a potential density above 27.5 kg/m^3 is considerably increased in OM10 and OM5 with respect to OM20 (see Fig. 16b). The distribution of water masses being transformed in OM10 and OM5 is shifted towards higher density waters. The transformation of Dense Shelf Water (waters denser than 27.80 kg/m^3, as in Kusahara et al. (2011b)) is much lower in OM20 (0.04 Sv) compared to OM10 and OM5 (0.31 Sv and 0.39 Sv, respectively). Under higher-resolution forcing, there is a clear shift towards higher rates of dense water production, and towards the production of denser waters. A notable result from this analysis is the similarity between OM10 and OM5 regarding water mass transformation rates. This is in line with the fact that the increase in sea ice production is weaker between OM10 and OM5 compared to that between OM10 and OM20.

A second important contributor to the salinity budget in coastal seas of Antarctica is the freshwater flux from ice shelf melt. Ocean–ice shelf interactions at the ice shelf base can for instance transform Shelf Waters into lighter water masses (Huot et al., 2021). The total ice shelf basal melt simulated in the OM20, OM10 and OM5 simulations are shown in Fig. 17. The three experiments have similar ice shelf basal melts between 2010 and 2013. After 2013, the ice shelf melt is increased by 1×10^{-4} Sv in OM20 compared to OM10 and OM5, while OM10 and OM5 have identical basal melts. Integrated over the pink box of Fig. 1, the ice shelf melt is decreased from 14.01 Gt/yr to 13.08 Gt/yr (−7.1%) between OM20 and OM5, which only partially offset the increase of sea ice production from 191.09 Gt/yr to 237.50 Gt/yr (+24.3%). Ice shelf basal melt is linked to the polynya activity as the ice shelf melt rate depends on the temperature of the water entering the ice shelf cavities. The production of cold and saline waters in polynyas can thus limit the basal melt of the neighboring ice shelf. As OM20 produces less sea ice and less Shelf Waters, less cold waters enter the ice shelf cavities and the ice shelf basal melt is higher than in OM10 and OM5. The similarities of ice shelf basal melt between OM10 and OM5 can be related to their similar rate of production of Shelf Waters (Fig. 16b). The increase of production of Shelf Waters in OM10 or OM5 compared to OM20 is reinforced by the weaker consumption of these water masses via ocean–ice shelf interactions. Increasing the atmospheric forcing resolution affects the Dense Water budget in two ways: it increases the production of Dense Water thanks to the intensification of polynya activity and it decreases the consumption of Dense Water through ocean–ice shelf interactions by decreasing the ice shelf melt rate.

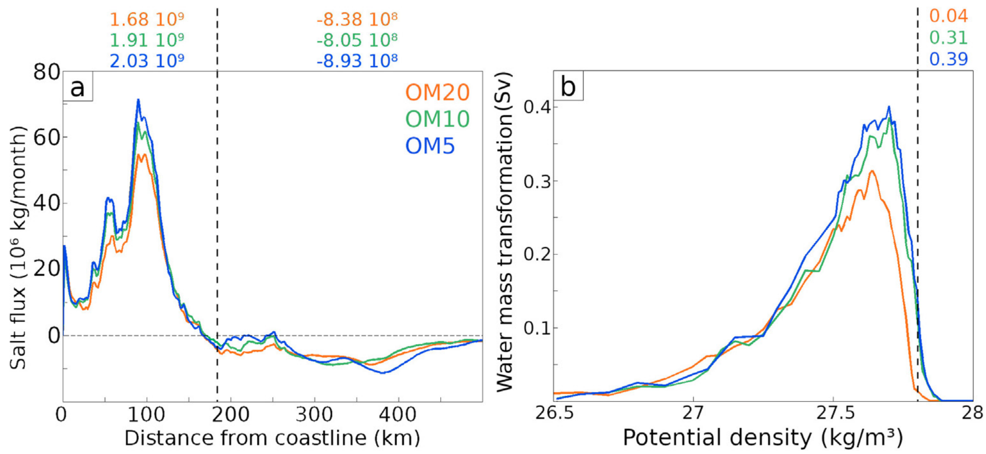

Fig. 16. (a) Meridional section of the yearly salt fluxes due to brine rejection or sea ice melting, averaged between 2010–2015. The vertical dashed line indicates the transition between positive (left) and negative (right) salt fluxes used to compute the total salt fluxes (numbers on top, in kg/month). (b) Mean water mass transformation rates by surface buoyancy fluxes per potential density class (potential density referenced to the surface). The dashed line indicates potential density anomaly σ_0 = 27.80 kg/m^3, i.e. the lowest density for Shelf Waters (which includes Dense Shelf Water) set following Kusahara et al. (2011b). Total shelf water transformation rates are listed on top of the diagram (in Sv). The diagnostics are computed from OM20, OM10, and OM5 outputs on the whole sector for panel (a) and in the box "east" (see Fig. 1) for panel (b).

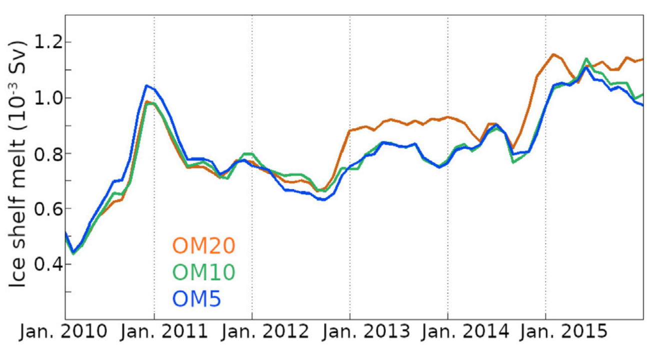

Fig. 17. Total ice shelf basal melt in the Adélie Land sector simulated in OM20, OM10 and OM5.

6. Discussion

This study examined the sensitivity of winds, sea ice, and ocean salt fluxes off Adélie Land to an increase in resolution of the atmospheric model and forcing beyond the resolution of present global reanalyses. To do so, we have performed a set of regional atmospheric simulations at 20, 10, and 5 km resolutions. These experiments revealed that katabatic winds are intensified and extend further offshore when the atmospheric resolution is increased. At higher resolution, the offshore component of the winds (perpendicular to the coastline) is intensified. The changes in wind speed and direction were attributed to the better representation of the steep continental slopes and of the valleys channelizing the katabatic flow. The three atmospheric simulations were then used to force a 1/24° resolution regional ocean–sea ice model. Due to the higher wind speed and wind-driven sea ice divergence, sea ice production is substantially increased under higher-resolution forcing, especially in polynyas. Polynyas are larger and produce up to 30% more sea ice when using a 5 km instead of a 20 km forcing resolution. Yet, each polynya presents a distinct sensitivity to forcing resolution depending on the local wind conditions, with coastal polynyas being more sensitive than those located further offshore. The increase in sea ice production with higher resolution forcing affects the salinity budget over the whole Adélie Land sector and intensifies the production of Dense Shelf Water. These results demonstrate the sensitivity of coastal sea ice to small-scale atmospheric processes.

The results presented here suggest that simulated coastal polynyas are highly sensitive to the resolution of the atmospheric forcing. The use of coarse-resolution forcing might be a limitation for sea ice and ocean modeling off Antarctica. As mentioned earlier, many regional high-resolution models are forced by relatively coarse-resolution global atmospheric reanalyses (Marsland et al., 2004, 2007; Kusahara et al., 2011a; Cougnon et al., 2013; Kusahara et al., 2017; Cougnon et al., 2017; Donat-Magnin et al., 2017; Huot et al., 2021). Despite the recent increase in horizontal resolution of these reanalyses, our results indicate that the use of higher-resolution forcing intensifies the activity of coastal polynyas, which are crucial for the air-sea-ice exchanges in the coastal Southern Ocean. It has to be noted that using ERA5 as atmospheric forcing leads to similar sea ice production rates than our experiment OM5 (see Appendix A), but this was attributed to differences in the physics of both models and does not undermine our conclusions about the effects of resolution. However, it is worth mentioning that most of the impact of the forcing resolution is already achieved at a horizontal resolution of 10 km. We found that the intensification of wind speeds and sea ice production in response to an increase in the atmospheric model resolution are higher between 20 km and 10 km resolution than between 10 km and 5 km resolution. The increase in dense water production with forcing resolution becomes even insignificant between OM10 and OM5. Dividing the resolution of the atmospheric by a factor 2 has a stronger impact from 20 to 10 km resolution than from 10 to 5 km resolution.

The Adélie Land sector has a relatively smooth topography compared to mountainous regions of Antarctica, suggesting that our conclusion about the role of forcing resolution can be extended to other sectors of Antarctica with similar topography. The 10 km resolution appears as a reasonable compromise between realism and computational cost for the forcing of coastal sea ice and ocean models. The use of higher resolutions could remain necessary for the study of certain areas, such as the coastal polynyas off the Mertz and Ninnis glaciers, or in mountainous areas of Antarctica such as the Antarctic Peninsula (Petrelli et al., 2008; Ebner et al., 2014). Another way of accounting for these locally intense winds is to correct global reanalyses using a higher-resolution regional model, as proposed by Mathiot et al. (2010). Such method is supported by the results from our experiment OM5x20, as coarsening the high-resolution atmospheric forcing yields only minor changes. Finally, the sensitivity of the ocean and sea ice to atmospheric forcing resolution would also most likely depend upon the resolution of the ocean grid itself, and on the representation of grounded icebergs and landfast ice.

Under higher wind speeds, the sea ice production in coastal polynyas drastically increases (e.g., +30% for the MGP and NGP for a +15% intensification of the wind speed). This implies some precautions for the estimation of the sea ice production in polynyas from remote sensing data. Tamura et al. (2016) constructed a valuable dataset gathering the sea ice growth rates in coastal polynyas off Antarctica. However, their estimates rely on coarse-resolution atmospheric reanalyses, probably simulating too weak winds down katabatic corridors. Our results suggest that their sea ice growth rates might be significantly underestimated for some polynyas, such as the Mertz and Ninnis glacier polynyas as MAR produces stronger and more realistic winds than the ERA5 global reanalysis in these areas.

The katabatic winds of Adélie Land appear to be highly sensitive to the resolution of the atmospheric model. However, our experiments only consider part of the response of the atmosphere to an increase in resolution. Indeed, the sea ice concentrations and sea surface temperatures are identical in the three atmospheric simulations. The role of small-scale spatial heterogeneity of the sea ice cover is for instance not accounted for. In addition, the atmosphere only partially responds to the increased air-sea heat flux in polynyas due to the wind intensification, as the sea ice conditions are prescribed in MAR. The intensification of heat, moisture, and momentum exchanges due to the enlargement of the polynyas would warm and moisten the air, potentially destabilizing the air column and thus affecting atmospheric convection (Weijer et al., 2017). Air-sea interactions above polynyas have been shown to produce breeze-like circulations that can intensify the downslope katabatic winds (Gallée, 1997; Savijärvi, 2011), but would also warm and saturate the air with water vapor, further increasing the snow accumulation over the ice sheet (Kittel et al., 2018). The impact of these processes on the activity of polynyas can be significant (Jourdain et al., 2011), but are not accounted for in our forced experiments.

7. Conclusion

Our results show that the representation of small-scale coastal winds, essential for the activity of coastal polynyas, strongly depends upon the atmospheric model resolution in the Adélie Land sector. At higher resolution, katabatic winds are shown to be significantly swifter and to extend further offshore. These changes increase the size of polynyas and enhance sea ice production by up to 30%. Larger volumes of sea ice are produced in coastal seas under high-resolution forcing, affecting the salinity budget of the Southern Ocean and the production of Dense Shelf Water. Thus, we conclude that air-sea-ice interactions in coastal Antarctica are highly sensitive to the resolution of the atmospheric forcing. Our results suggest that a resolution of 10 km might be needed to force an ocean–sea ice model off Adélie Land and potentially other sectors of Antarctica. Further resolution refinement yields locally significant impacts but has minor effects on the sector-averaged salt budget and water mass transformations.

While the importance of polynyas for polar climate is indubitable, further work is needed to understand their driving mechanisms and to find a suitable approach to incorporate them in global climate models. The high sensitivity of polynya activity and dense water formation to the local wind questions their response to future atmospheric circulation changes in Antarctica such as the projected shift in Southern Ocean westerlies (Spence et al., 2014; Hazel and Stewart, 2019) which could affect the evolution of katabatic and easterlies in a warmer climate. The response of polynyas to the modification of the atmospheric conditions with climate change is an important question, as changes in polynya activity would have far-reaching consequences for the global ocean circulation and ice sheet mass balance. In parallel, the importance of feedbacks between the ocean, ice, and air above polynyas remains mostly unknown and would require further work using high-resolution coupled atmosphere–sea-ice–ocean models.

CRediT authorship contribution statement

Pierre-Vincent Huot: Conceptualization, Methodology, Formal analysis, Investigation, Writing – original draft, Writing – review and editing. **Christoph Kittel:** Methodology, Formal analysis, Writing – original draft, Writing – review and editing. **Thierry Fichefet:** Conceptualization, Supervision, Writing – review and editing. **Nicolas C. Jourdain:** Supervision, Writing – review and editing. **Jean Sterlin:** Methodology, Writing – review and editing. **Xavier Fettweis:** Supervision, Writing – review and editing.

Declaration of competing interest

The authors declare that they have no known competing financial interests or personal relationships that could have appeared to influence the work reported in this paper.

Acknowledgments

The authors are thankful to the two anonymous reviewers who helped to improve the manuscript. This research was conducted within the F.R.S.-FNRS PDR T.0002.16 "Air-Ice-Ocean Interactions in Antarctica" and the PARAMOUR project, funded by the Research Foundation-Flanders (Research Foundation – Flanders (FWO)) and F.R.S.-FNRS under the Excellence of Science (EOS) programme (grant EOS O0100718F). Computational resources have been provided by the supercomputing facilities of the Université catholique de Louvain (CISM/UCL) and the Consortium des Équipements de Calcul Intensif en Fédération Wallonie Bruxelles (CÉCI) funded by the Fond de la Recherche Scientifique de Belgique (F.R.S.-FNRS) under convention 2.5020.11. The present research benefited from computational resources made available on the Tier-1 supercomputer of the Fédération Wallonie-Bruxelles, infrastructure funded by the Walloon Region under the grant agreement n° 1117545.

Appendix A. Comparison between MAR-forced and ERA5-forced simulations

Supplementary material related to this article can be found online at https://doi.org/10.1016/j.ocemod.2021.101901.

References

Abernathey, R.P., Cerovecki, I., Holland, P.R., Newsom, E., Mazloff, M., Talley, L.D., 2016. Water-mass transformation by sea ice in the upper branch of the Southern Ocean overturning. Nat. Geosci. 9, 596–601.
Agosta, C., Amory, C., Kittel, C., Orsi, A., Favier, V., Gallée, H., van den Broeke, M.R., Lenaerts, J., van Wessem, J.M., van de Berg, W.J., et al., 2019. Estimation of the antarctic surface mass balance using the regional climate model MAR (1979–2015) and identification of dominant processes. Cryosphere 13, 281–296.
Amory, C., Trouvilliez, A., Gallée, H., Favier, V., Naaim-Bouvet, F., Genthon, C., Agosta, C., Piard, L., Bellot, H., 2015. Comparison between observed and simulated aeolian snow mass fluxes in Adélie Land, East Antarctica.
Aoki, S., Kobayashi, R., Rintoul, S., Tamura, T., Kusahara, K., 2017. Changes in water properties and flow regime on the continental shelf off the A délie/G eorge VL and coast, E ast A ntarctica, after glacier tongue calving. J. Geophys. Res. Oceans 122, 6277–6294.
Barthélemy, A., Goosse, H., Mathiot, P., Fichefet, T., 2012. Inclusion of a katabatic wind correction in a coarse-resolution global coupled climate model. Ocean Model. 48, 45–54.
Beaman, R.J., O'Brien, P.E., Post, A.L., D. Santis, L., 2011. A new high-resolution bathymetry model for the Terre Adélie and George V continental margin, East Antarctica. Antarct. Sci. 23, 95–103.
van de Berg, W.J., Medley, B., 2016. Brief communication: Upper-air relaxation in RACMO2 significantly improves modelled interannual surface mass balance variability in Antarctica. Cryosphere 10, 459–463.
Bougeault, P., Lacarrere, P., 1989. Parameterization of orography-induced turbulence in a mesobeta-scale model. Mon. Weather Rev. 117, 1872–1890.
Bromwich, D.H., Otieno, F.O., Hines, K.M., Manning, K.W., Shilo, E., 2013. Comprehensive evaluation of polar weather research and forecasting model performance in the Antarctic. J. Geophys. Res.: Atmos. 118, 274–292.

Brun, E., David, P., Sudul, M., Brunot, G., 1992. A numerical model to simulate snow-cover stratigraphy for operational avalanche forecasting. J. Glaciol. 38, 13–22.

Carrère, L., Lyard, F., Cancet, M., Guillot, A., Roblou, L., 2012. A new global tidal model taking taking advantage of nearly 20 years of altimetry. In: Proceedings of meeting'' 20 Years of Altimetry.

Cougnon, E., Galton-Fenzi, B., Meijers, A., Legrésy, B., 2013. Modeling interannual dense shelf water export in the region of the Mertz Glacier Tongue (1992–2007). J. Geophys. Res. Oceans 118, 5858–5872.

Cougnon, E., Galton-Fenzi, B., Rintoul, S., Legrésy, B., Williams, G., Fraser, A., Hunter, J., 2017. Regional changes in icescape impact shelf circulation and basal melting. Geophys. Res. Lett. 44.

De Ridder, K., Gallée, H., 1998. Land surface–induced regional climate change in southern Israel. J. Appl. Meteorol. 37, 1470–1485.

Dinniman, M.S., Klinck, J.M., Bai, L.S., Bromwich, D.H., Hines, K.M., Holland, D.M., 2015. The effect of atmospheric forcing resolution on delivery of ocean heat to the Antarctic floating ice shelves. J. Clim. 28, 6067–6085.

Donat-Magnin, M., Jourdain, N.C., Gallée, H., Amory, C., Kittel, C., Fettweis, X., Wille, J.D., Favier, V., Drira, A., Agosta, C., 2020. Interannual variability of summer surface mass balance and surface melting in the Amundsen sector, West Antarctica. Cryosphere.

Donat-Magnin, M., Jourdain, N.C., Spence, P., L. Sommer, J., Gallée, H., Durand, G., 2017. Ice-shelf melt response to changing winds and glacier dynamics in the Amundsen Sea Sector, Antarctica. J. Geophys. Res. Oceans 122, 10206–10224.

Dumont, D., Gratton, Y., Arbetter, T.E., 2009. Modeling the dynamics of the North Water polynya ice bridge. J. Phys. Oceanogr. 39, 1448–1461.

Ebner, L., Heinemann, G., Haid, V., Timmermann, R., 2014. Katabatic winds and polynya dynamics at Coats Land, Antarctica. Antarct. Sci. 26, 309–326.

Engedahl, H., 1995. Use of the flow relaxation scheme in a three-dimensional baroclinic ocean model with realistic topography. Tellus A 47, 365–382.

Flather, R.A., 1994. A storm surge prediction model for the northern bay of bengal with application to the cyclone disaster in April 1991. J. Phys. Oceanogr. 24, 172–190.

Fraser, A.D., Massom, R.A., Michael, K.J., Galton-Fenzi, B.K., Lieser, J.L., 2012. East Antarctic landfast sea ice distribution and variability, 2000–08. J. Clim. 25, 1137–1156.

Fraser, A.D., Ohshima, K.I., Nihashi, S., Massom, R.A., Tamura, T., Nakata, K., Williams, G.D., Carpentier, S., Willmes, S., 2019. Landfast ice controls on sea-ice production in the Cape Darnley Polynya: A case study. Remote Sens. Environ. 233, 111315.

Fretwell, P., Pritchard, H.D., Vaughan, D.G., Bamber, J., Barrand, N., Bell, R., Bianchi, C., Bingham, R., Blankenship, D.D., Casassa, G., et al., 2013. Bedmap2: improved ice bed, surface and thickness datasets for Antarctica.

Gallée, H., 1995. Simulation of the mesocyclonic activity in the Ross Sea, Antarctica. Mon. Weather Rev. 123, 2051–2069. http://dx.doi.org/10.1175/1520-0493(1995)123<2051:SOTMAI>2.0.CO;2.

Gallée, H., 1997. Air-sea interactions over Terra Nova Bay during winter: Simulation with a coupled atmosphere-polynya model. J. Geophys. Res.: Atmos. 102, 13835–13849.

Gallée, H., Duynkerke, P.G., 1997. Air-snow interactions and the surface energy and mass balance over the melting zone of west Greenland during the Greenland Ice Margin Experiment. J. Geophys. Res.: Atmos. 102, 13813–13824.

Gallée, H., Guyomarc'h, G., Brun, E., 2001. Impact of snow drift on the Antarctic ice sheet surface mass balance: possible sensitivity to snow-surface properties. Bound.-Lay. Meteorol. 99, 1–19.

Gallée, H., Preunkert, S., Argentini, S., Frey, M.M., Genthon, C., Jourdain, B., Pietroni, I., Casasanta, G., Barral, H., Vignon, E., 2015. Characterization of the boundary layer at Dome C (East Antarctica) during the OPALE summer campaign. Atmos. Chem. Phys. 15, 6225–6236.

Gallée, H., Schayes, G., 1994. Development of a three-dimensional meso-γ primitive equation model: katabatic winds simulation in the area of Terra Nova Bay, Antarctica. Mon. Weather Rev. 122, 671–685.

Gaspar, P., Grégoris, Y., Lefevre, J.M., 1990. A simple eddy kinetic energy model for simulations of the oceanic vertical mixing: Tests at station Papa and Long-Term Upper Ocean Study site. J. Geophys. Res. Oceans 95, 16179–16193.

Guerreiro, K., Fleury, S., Zakharova, E., Kouraev, A., Rémy, F., Maisongrande, P., 2017. Comparison of CryoSat-2 and ENVISAT radar freeboard over Arctic sea ice: towards an improved Envisat freeboard retrieval. Cryosphere 11 (2059).

Hausmann, U., Sallée, J.B., Jourdain, N., Mathiot, P., Rousset, C., Madec, G., Deshayes, J., 2020. Interannual tidal signatures in iceshelf melt in a new NEMO-LIM3 configuration of the southwestern Weddell Gyre, its shelves and sub-iceshelf seas. In: Geophysical Research Abstracts.

Hazel, J.E., Stewart, A.L., 2019. Are the near-antarctic easterly winds weakening in response to enhancement of the Southern Annular Mode? J. Clim. 32, 1895–1918.

Hersbach, H., Bell, B., Berrisford, P., Hirahara, S., Horányi, A., Muñoz Sabater, J., Nicolas, J., Peubey, C., Radu, R., Schepers, D., et al., 2020. The ERA5 global reanalysis. Q. J. R. Meteorol. Soc. 146, 1999–2049.

Heuzé, C., 2020. Antarctic bottom water and north Atlantic deep water in CMIP6 models. Ocean Sci. Discuss. 1–38.

Heuzé, C., Heywood, K.J., Stevens, D.P., Ridley, J.K., 2013. Southern Ocean bottom water characteristics in CMIP5 models. Geophys. Res. Lett. 40, 1409–1414.

Huot, P.V., Fichefet, T., Jourdain, N.C., Mathiot, P., Rousset, C., Kittel, C., Fettweis, X., 2021. Influence of ocean tides and ice shelves on ocean-ice interactions and dense shelf water formation in the D'Urville Sea, Antarctica. Ocean Modelling 162, http://dx.doi.org/10.1016/j.ocemod.2021.101794.

Jacobs, S., Helmer, H., Doake, C., Jenkins, A., Frolich, R., 1992. Melting of ice shelves and the mass balance of Antarctica. J. Glaciol. 38, 375–387.

Jeong, H., Asay-Davis, X.S., Turner, A.K., Comeau, D.S., Price, S.F., Abernathey, R.P., Veneziani, M., Petersen, M.R., Hoffman, M.J., Mazloff, M.R., et al., 2020. Impacts of ice-shelf melting on water-mass transformation in the southern ocean from E3SM simulations. J. Clim. 33, 5787–5807.

Jourdain, N.C., Gallée, H., 2011. Influence of the orographic roughness of glacier valleys across the Transantarctic Mountains in an atmospheric regional model. Clim. Dynam. 36, 1067–1081.

Jourdain, N.C., Mathiot, P., Gallée, H., Barnier, B., 2011. Influence of coupling on atmosphere, sea ice and ocean regional models in the Ross Sea sector, Antarctica. Clim. Dynam. 36, 1523–1543.

Jourdain, N.C., Mathiot, P., Merino, N., Durand, G., L. Sommer, J., Spence, P., Dutrieux, P., Madec, G., 2017. Ocean circulation and sea-ice thinning induced by melting ice shelves in the Amundsen Sea. J. Geophys. Res. Oceans 122, 2550–2573.

Jourdain, N.C., Molines, J.M., L. Sommer, J., Mathiot, P., Chanut, J., d. Lavergne, C., Madec, G., 2019. Simulating or prescribing the influence of tides on the Amundsen Sea ice shelves. Ocean Model. 133, 44–55.

Kessler, E., 1969. On the distribution and continuity of water substance in atmospheric circulations. In: On the Distribution and Continuity of Water Substance in Atmospheric Circulations. Springer, pp. 1–84.

Kittel, C., Amory, C., Agosta, C., Delhasse, A., Doutreloup, S., Huot, P.V., Wyard, C., Fichefet, T., Fettweis, X., 2018. Sensitivity of the current Antarctic surface mass balance to sea surface conditions using MAR. Cryosphere 12, 3827–3839.

König Beatty, C., Holland, D.M., 2010. Modeling landfast sea ice by adding tensile strength. J. Phys. Oceanogr. 40, 185–198.

Kusahara, K., Hasumi, H., Fraser, A.D., Aoki, S., Shimada, K., Williams, G.D., Massom, R., Tamura, T., 2017. Modeling ocean–cryosphere interactions off Adélie and George V Land, East Antarctica. J. Clim. 30, 163–188. http://dx.doi.org/10.1175/jcli-d-15-0808.1.

Kusahara, K., Hasumi, H., Williams, G.D., 2011a. Dense shelf water formation and brine-driven circulation in the Adélie and George V Land region. Ocean Model. 37, 122–138.

Kusahara, K., Hasumi, H., Williams, G.D., 2011b. Impact of the Mertz Glacier Tongue calving on dense water formation and export. Nature Commun. 2 (159).

Labrousse, S., Williams, G., Tamura, T., Bestley, S., Sallée, J.B., Fraser, A.D., Sumner, M., Roquet, F., Heerah, K., Picard, B., et al., 2018. Coastal polynyas: Winter oases for subadult southern elephant seals in East Antarctica. Sci. Rep. 8, 1–15.

Lacarra, M., Houssais, M.N., Herbaut, C., Sultan, E., Beauverger, M., 2014. Dense shelf water production in the Adélie Depression, East Antarctica, 2004–2012: Impact of the Mertz Glacier calving. J. Geophys. Res. Oceans 119, 5203–5220. http://dx.doi.org/10.1002/2013jc009124.

Large, W.G., Yeager, S.G., 2004. Diurnal to decadal global forcing for ocean and sea-ice models: the data sets and flux climatologies.

Le Toumelin, L., Amory, C., Favier, V., Kittel, C., Hofer, S., Fettweis, X., Gallée, H., Kayetha, V., 2020. Sensitivity of the surface energy budget to drifting snow as simulated by MAR in coastal Adelie Land, Antarctica. Cryosphere Discuss. 1–27.

Lecomte, O., Goosse, H., Fichefet, T., Holland, P.R., Uotila, P., Zunz, V., Kimura, N., 2016. Impact of surface wind biases on the Antarctic sea ice concentration budget in climate models. Ocean Model. 105, 60–70. http://dx.doi.org/10.1016/j.ocemod.2016.08.001.

Lefebre, F., Gallée, H., Ypersele, Greuell, W., 2003. Modeling of snow and ice melt at ETH Camp (West Greenland): A study of surface albedo. J. Geophys. Res.: Atmos. 108, http://dx.doi.org/10.1029/2001JD001160.

Lemieux, 2016. Improving the simulation of landfast ice by combining tensile strength and a parameterization for grounded ridges.

Lin, Y.L., Farley, R.D., Orville, H.D., 1983. Bulk parameterization of the snow field in a cloud model. J. Appl. Meteorol. Climatol. 22, 1065–1092.

Liniger, G., Strutton, P.G., Lannuzel, D., Moreau, S., 2020. Calving event led to changes in phytoplankton bloom phenology in the Mertz polynya, Antarctica. J. Geophys. Res. Oceans e2020JC016387.

Madec, G., 2016. NEMO Ocean Engine. Note Du Pôle de modélisation. (27), Institut Pierre-Simon Laplace (IPSL), France, (ISSN: 1288-1619).

Maraldi, C., Chanut, J., Levier, B., Ayoub, N., D. Mey, P., Reffray, G., Lyard, F., Cailleau, S., Drévillon, M., Fanjul, E., et al., 2013. NEMO on the shelf: assessment of the Iberia-Biscay-Ireland configuration.

Marchi, S., Fichefet, T., Goosse, H., Zunz, V., Tietsche, S., Day, J.J., Hawkins, E., 2019. Reemergence of Antarctic sea ice predictability and its link to deep ocean mixing in global climate models. Clim. Dynam. 52, 2775–2797.

Marsland, S.J., Bindoff, N., Williams, G., Budd, W., 2004. Modeling water mass formation in the Mertz Glacier Polynya and Adélie Depression, east Antarctica. J. Geophys. Res. Oceans 109.

Marsland, S.J., Church, J.A., Bindoff, N.L., Williams, G.D., 2007. Antarctic coastal polynya response to climate change. J. Geophys. Res. Oceans 112, http://dx.doi.org/10.1029/2005JC003291.

Martin, A., Houssais, M.N., Goff, H.L., Marec, C., Dausse, D., 2017. Circulation and water mass transports on the East Antarctic shelf in the Mertz Glacier region. Deep Sea Res. I 126, 1–20. http://dx.doi.org/10.1016/j.dsr.2017.05.007.

Massom, R., Harris, P., Michael, K.J., Potter, M., 1998. The distribution and formative processes of latent-heat polynyas in East Antarctica. Ann. Glaciol. 27, 420–426.

Mathiot, P., Barnier, B., Gallée, H., Molines, J.M., Sommer, J.L., Juza, M., Penduff, T., 2010. Introducing katabatic winds in global ERA40 fields to simulate their impacts on the Southern Ocean and sea-ice. Ocean Model. 35, 146–160. http://dx.doi.org/10.1016/j.ocemod.2010.07.001.

Mathiot, P., Jenkins, A., Harris, C., Madec, G., 2017. Explicit representation and parametrised impacts of under ice shelf seas in the z* coordinate ocean model NEMO 3.6. Geosci. Model Dev. 10, 2849–2874. http://dx.doi.org/10.5194/gmd-10-2849-2017.

Mathiot, P., Jourdain, N.C., Barnier, B., Gallée, H., Molines, J.M., Sommer, J.L., Penduff, T., 2012. Sensitivity of coastal polynyas and high-salinity shelf water production in the Ross Sea, Antarctica, to the atmospheric forcing. Ocean Dyn. 62, 701–723. http://dx.doi.org/10.1007/s10236-012-0531-y.

Mayet, C., Testut, L., Legresy, B., Lescarmontier, L., Lyard, F., 2013. High-resolution barotropic modeling and the calving of the Mertz Glacier, East Antarctica. J. Geophys. Res. Oceans 118, 5267–5279. http://dx.doi.org/10.1002/jgrc.20339.

Merino, N., Sommer, J.L., Durand, G., Jourdain, N.C., Madec, G., Mathiot, P., Tournadre, J., 2016. Antarctic icebergs melt over the Southern Ocean: Climatology and impact on sea ice. Ocean Model. 104, 99–110. http://dx.doi.org/10.1016/j.ocemod.2016.05.001.

Morale Maqueda, M., Willmott, A., Biggs, N., 2004. Polynya dynamics: A review of observations and modeling. Rev. Geophys. 42.

Morcrette, J.J., 2002. The surface downward longwave radiation in the ECMWF forecast system. J. Clim. 15, 1875–1892. http://dx.doi.org/10.1175/1520-0442(2002)015<1875:TSDLRI>2.0.CO;2.

Mottram, R., Hansen, N., Kittel, C., van Wessem, M., Agosta, C., Amory, C., Boberg, F., van de Berg, W.J., Fettweis, X., Gossart, A., et al., 2020. What is the surface mass balance of antarctica? An intercomparison of regional climate model estimates. Cryosphere Discuss. 1–42.

Nihashi, S., Ohshima, K.I., 2015. Circumpolar mapping of Antarctic Coastal polynyas and landfast sea ice: Relationship and variability. J. Clim. 28, 3650–3670. http://dx.doi.org/10.1175/jcli-d-14-00369.1.

Parish, T.R., Bromwich, D.H., 1987. The surface windfield over the Antarctic ice sheets. Nature 328, 51–54.

Petrelli, P., Bindoff, N., Bergamasco, A., 2008. The sea ice dynamics of Terra Nova Bay and Ross Ice Shelf Polynyas during a spring and winter simulation. J. Geophys. Res. Oceans 113.

Rintoul, S.R., 1998. On the origin and influence of Adélie Land Bottom Water. In: Ocean, Ice, and Atmosphere: Interactions At the Antarctic Continental Margin, Vol. 75. pp. 151–171.

Roquet, F., Madec, G., Brodeau, L., Nycander, J., 2015. Defining a simplified yet "realistic" equation of state for seawater. J. Phys. Oceanogr. 45, 2564–2579.

Rousset, C., Vancoppenolle, M., Madec, G., Fichefet, T., Flavoni, S., Barthélemy, A., Benshila, R., Chanut, J., Levy, C., Masson, S., Vivier, F., 2015. The Louvain-La-Neuve sea ice model LIM3.6: global and regional capabilities. Geosci. Model Dev. 8, 2991–3005. http://dx.doi.org/10.5194/gmd-8-2991-2015.

Savijärvi, H., 2011. Antarctic local wind dynamics and polynya effects on the Adélie Land coast. Q. J. R. Meteorol. Soc. 137, 1804–1811.

Snow, K., Rintoul, S.R., Sloyan, B.M., Hogg, A.M., 2018. Change in dense shelf water and Adélie land bottom water precipitated by iceberg calving. Geophys. Res. Lett. 45, 2380–2387. http://dx.doi.org/10.1002/2017gl076195.

Spence, P., Griffies, S.M., England, M.H., Hogg, A.M., Saenko, O.A., Jourdain, N.C., 2014. Rapid subsurface warming and circulation changes of Antarctic coastal waters by poleward shifting winds. Geophys. Res. Lett. 41, 4601–4610. http://dx.doi.org/10.1002/2014gl060613.

Spreen, G., Kaleschke, L., Heygster, G., 2008. Sea ice remote sensing using AMSR-e 89-GHz channels. J. Geophys. Res. Oceans 113.

Tamura, T., Ohshima, K.I., Fraser, A.D., Williams, G.D., 2016. Sea ice production variability in Antarctic coastal polynyas. J. Geophys. Res. Oceans 121, 2967–2979.

Tamura, T., Williams, G.D., Fraser, A.D., Ohshima, K.I., 2012. Potential regime shift in decreased sea ice production after the Mertz Glacier calving. Nature Commun. 3, http://dx.doi.org/10.1038/ncomms1820.

Tetzner, D., Thomas, E., Allen, C., 2019. A validation of ERA5 reanalysis data in the Southern Antarctic Peninsula–Ellsworth Land Region, and its implications for ice core studies. Geosciences 9, 289.

Uppala, S.M., KÅllberg, P.W., Simmons, A.J., Andrae, U., Bechtold, V.D.C., Fiorino, M., Gibson, J.K., Haseler, J., Hernandez, A., Kelly, G.A., Li, X., Onogi, K., Saarinen, S., Sokka, N., Allan, R.P., Andersson, E., Arpe, K., Balmaseda, M.A., Beljaars, A.C.M., Berg, L.V.D., Bidlot, J., Bormann, N., Caires, S., Chevallier, F., Dethof, A., Dragosavac, M., Fisher, M., Fuentes, M., Hagemann, S., Hólm, E., Hoskins, B.J., Isaksen, L., Janssen, P.a. E.M., Jenne, R., Mcnally, A.P., Mahfouf, J.F., Morcrette, J.J., Rayner, N.A., Saunders, R.W., Simon, P., Sterl, A., Trenberth, K.E., Untch, A., Vasiljevic, D., Viterbo, P., Woollen, J., 2005. The ERA-40 re-analysis. Q. J. R. Meteorol. Soc. 131, 2961–3012. http://dx.doi.org/10.1256/qj.04.176.

Van Achter, G., Fichefet, T., Goosse, H., Pelletier, C., Huot, P.V., Sterlin, J., Fraser, A.D., Parter-Smith, R., Lemieux, J.F., Haubner, K., 2021. Modelling landfast sea ice and its influence on ocean-ice interactions in the area of the Totten Glacier, East Antarctica. Ocean Model. (Submitted).

Vancoppenolle, M., Fichefet, T., Goosse, H., Bouillon, S., Madec, G., Maqueda, M.A.M., 2009. Simulating the mass balance and salinity of Arctic and Antarctic sea ice. 1. Model description and validation. Ocean Model. 27, 33–53. http://dx.doi.org/10.1016/j.ocemod.2008.10.005.

Weatherall, P., Marks, K.M., Jakobsson, M., Schmitt, T., Tani, S., Arndt, J.E., Rovere, M., Chayes, D., Ferrini, V., Wigley, R., 2015. A new digital bathymetric model of the world oceans. Earth Space Sci. 2, 331–345. http://dx.doi.org/10.1002/2015ea000107.

Weijer, W., Veneziani, M., Stössel, A., Hecht, M.W., Jeffery, N., Jonko, A., Hodos, T., Wang, H., 2017. Local atmospheric response to an open-ocean polynya in a high-resolution climate model. J. Clim. 30, 1629–1641.

Wendler, G., Stearns, C., Weidner, G., Dargaud, G., Parish, T., 1997. On the extraordinary katabatic winds of Adélie land. J. Geophys. Res.: Atmos. 102, 4463–4474.

Williams, G.D., Bindoff, N.L., Marsland, S.J., Rintoul, S.R., 2008. Formation and export of dense shelf water from the Adélie Depression, East Antarctica. J. Geophys. Res. 113, http://dx.doi.org/10.1029/2007jc004346.

Zhang, Z., Vihma, T., Stössel, A., Uotila, P., 2015. The role of wind forcing from operational analyses for the model representation of Antarctic coastal sea ice. Ocean Model. 94, 95–111.